ARTICLE

Nonmagnetic single-molecule spin-filter based on quantum interference

Atindra Nath Pal[1,2], Dongzhe Li[3], Soumyajit Sarkar [4], Sudipto Chakrabarti[1], Ayelet Vilan [1], Leeor Kronik[4], Alexander Smogunov[5] & Oren Tal [1]*

Key spin transport phenomena, including magnetoresistance and spin transfer torque, cannot be activated without spin-polarized currents, in which one electron spin is dominant. At the nanoscale, the relevant length-scale for modern spintronics, spin current generation is rather limited due to unwanted contributions from poorly spin-polarized frontier states in ferromagnetic electrodes, or too short length-scales for efficient spin splitting by spin-orbit interaction and magnetic fields. Here, we show that spin-polarized currents can be generated in silver-vanadocene-silver single molecule junctions without magnetic components or magnetic fields. In some cases, the measured spin currents approach the limit of ideal ballistic spin transport. Comparison between conductance and shot-noise measurements to detailed calculations reveals a mechanism based on spin-dependent quantum interference that yields very efficient spin filtering. Our findings pave the way for nanoscale spintronics based on quantum interference, with the advantages of low sensitivity to decoherence effects and the freedom to use non-magnetic materials.

[1] Department of Chemical and Biological Physics, Weizmann Institute of Science, Rehovot, Israel. [2] Department of Condensed Matter Physics and Material Sciences, S. N. Bose National Centre for Basic Sciences, Block JD, Sector III, Salt Lake, Kolkata, India. [3] Department of Physics, University of Konstanz, Konstanz, Germany. [4] Department of Materials and Interfaces, Weizmann Institute of Science, Rehovot, Israel. [5] SPEC, CEA, CNRS, Université Paris-Saclay, CEA Saclay, Cedex Gif-sur-Yvette, France. *email: oren.tal@weizmann.ac.il

Quantum interference is a fundamental quantum mechanical phenomenon with a variety of implications for metrology[1], quantum information processing[2], and chemical processes[3,4]. In nanoscale electronic devices, electron quantum interference is an attractive effect because it can be used to control electronic transport using strategies that are not accessible by traditional electronics. In recent years, quantum interference has been studied intensively in molecular junctions based on molecules suspended between two electrodes[5–19]. In a series of experiments complemented by calculations, it was shown that destructive interference between different current pathways across the molecular bridge efficiently suppresses the overall charge transport in the studied molecular junction[10–18]. Interestingly, the structure of the molecular bridge can be optimized to promote efficient destructive interference at the relevant energy for electronic transport, such that the bridging molecule can be a better insulator than a vacuum gap[16]. In contrast, constructive interference can cause the measured total conductance of two transport pathways across a molecular junction to be more than twice the conductance of each pathway[19]. Despite extensive experimental study of quantum interference in molecular junctions, the influence of quantum interference on spin transport in such junctions has not been demonstrated.

Here, we show that highly spin-polarized currents can be generated in paramagnetic molecular junctions without magnetic components or magnetic fields. Moreover, in some cases the obtained current approaches the limit of ideal ballistic spin transport. Specifically, using conductance and shot-noise measurements we detect spin-polarized currents in molecular junctions based on silver electrodes bridged by a vanadocene molecule. Some of the junctions show spin transport close to one quantum of spin conductance, which is dominated by an almost fully-open spin-polarized transmission channel. Detailed comparison between experimental findings and transport calculations reveals a mechanism based on spin-dependent quantum interference that yields very efficient spin filtering. Our findings pave the way for nanoscale spintronics based on quantum interference, with the advantages of low sensitivity to decoherence effects at the nanometer scale, and the freedom to use non-magnetic materials for faster, power-saving spin manipulations.

Results

Conductance measurements. The first single-molecule junctions considered here are based on individual vanadocene molecules suspended between two silver electrodes (Fig. 1a). The vanadocene molecule has a sandwich structure, with a core vanadium ion located between two cyclopentadienyl conjugated rings. In the gas phase, vanadocene has a total spin of $S = 3/2$[20], which is essentially preserved in the junction, as confirmed by our ab initio calculations.

We use a break-junction setup (Fig. 1b)[21] to form in situ molecular junctions in cryogenic vacuum conditions[22]. Specifically, two clean silver electrodes are prepared by breaking a silver wire at $4.2\,K$ into two segments with freshly exposed apices separated by a nanoscale gap (see Methods). Before the introduction of molecules, we verify the typical conductance of bare silver atomic junctions by repeatedly forming atomic-scale contacts between the electrode apices. Figure 1c, left panel shows examples for traces of conductance vs. inter electrodes displacement that were recorded during repeated breaking of the clean Ag junction. Before recording the next breaking conductance trace,
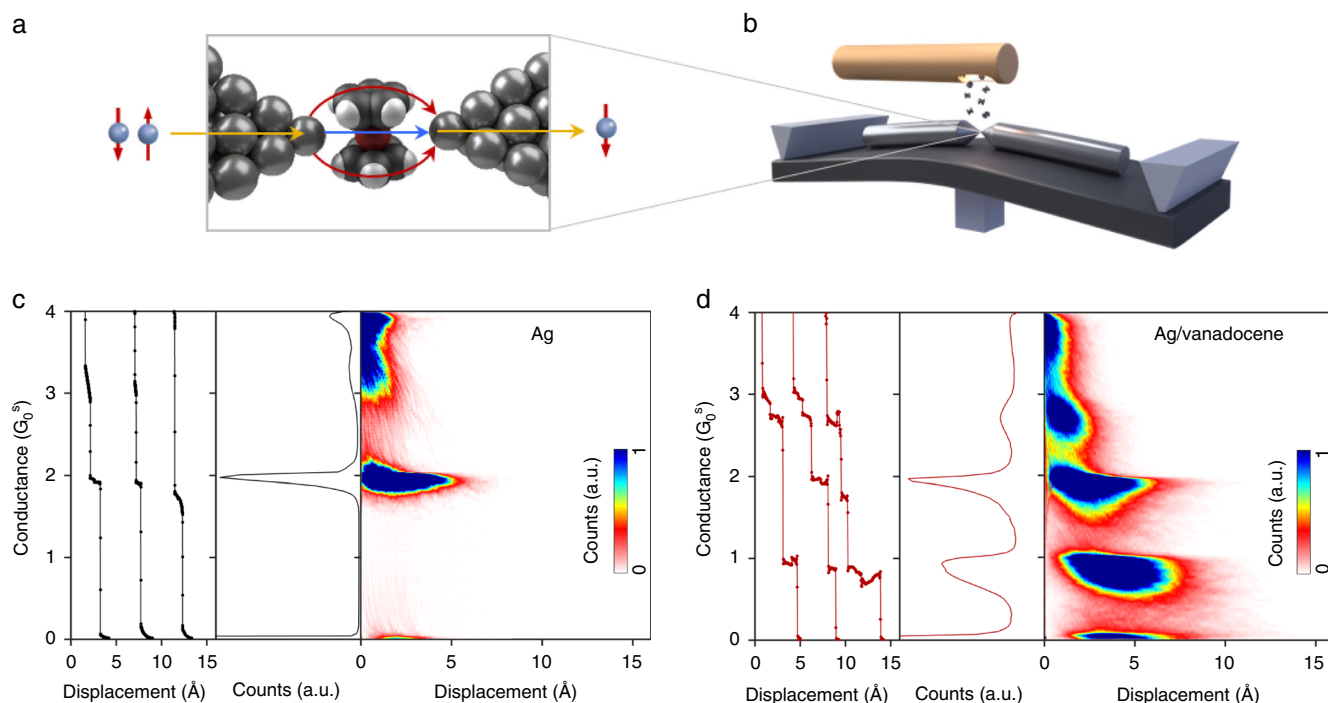

Fig. 1 Measured conductance of bare silver atomic-scale junctions and Ag/vanadocene molecular junctions. **a** Schematic representation of spin-filtering by interfering current pathways in a Ag/vanadocene single-molecule junction. **b** Schematics of the break-junction setup. **c** Characterization of bare silver atomic junctions. Left panel: examples for conductance versus inter-electrode displacement traces recorded at a bias voltage of 100 mV, with traces shifted in the displacement axis for clarity; Middle panel: conductance histogram constructed from 5,000 conductance traces; Right panel: conductance–displacement density plot based on the same conductance traces. **d** Similar characterization for Ag/vanadocene molecular junctions, with histograms based on the same number of traces. Zero displacement is determined for each conductance trace by the first displacement point with a conductance value below 4 G_0^s. Information on the measurement circuit can be found in Supplementary Note 1.

the junction is structurally deformed by pushing the electrode apices against each other to promote sampling of different junction structures. During the breaking process the conductance decreases and eventually a single silver atom contact is formed as indicated by a typical conductance plateau at ~2 G_0^s, ($G_0^s = e^2/h$ is the spin-polarized conductance quantum, where e is the electron charge, and h is Planck's constant)[21]. This value is given by two equal transmission channels for spin-up and down. Further elongation leads to junction breaking, followed by an abrupt conductance drop. The conductance histogram in Fig. 1c, middle panel, which is constructed from 5000 conductance traces, provides statistical information. The peak at ~2 G_0^s indicates that this is the most probable conductance of a silver atomic-scale junction, while the low conductance tail is the manifestation of tunneling transport after junction breaking. The conductance versus displacement density plot in Fig. 1c, right panel, presents the conductance evolution during the junction breaking process.

When vanadocene molecules are introduced to the junction from a local molecular source, additional plateaus appear at ~1 G_0^s (Fig. 1d, left panel). These plateaus indicate the formation of molecular junctions during the breaking process of the silver junction. Figure 1d, middle panel, presents a corresponding conductance histogram for the Ag/vanadocene junctions with a peak at ~2 G_0^s, as in the case of bare silver atomic junctions, and a new peak at ~1 G_0^s. The molecular origin of the lower conductance value is further verified by detecting the vibrational signature of the newly formed molecular junctions, using inelastic electron spectroscopy[23]. The conductance versus displacement density plot in Fig. 1d, right panel, shows the conductance evolution during the breaking process of the molecular junction. A conductance of 1 G_0^s, has been often regarded (incorrectly) as the smoking gun of fully spin-polarized conductance, namely conductance of only one spin type. For quantum coherent conductors, the conductance G is given by the Landauer formalism[24] as a sum of contributions from different spin-up and spin-down ($\sigma = \uparrow, \downarrow$) transmission channels, where the transmission of electrons via each spin-polarized channel has a probability $\tau_{i,\sigma}$ (i is the channel index), namely, $G = G_0^s \sum_{i,\sigma} \tau_{i,\sigma}$. The conductance is indeed 1 G_0^s for fully spin-polarized transport carried by a fully-open single spin channel ($\tau_\sigma = 1$). However, the same conductance can also be obtained by an arbitrary sum of partially open channels ($0 < \tau_{i,\sigma} < 1$), not necessarily of the same spin type. Thus, a conductance of 1 G_0^s is not a sufficient indicator for fully spin-polarized conductance and further information, such as the transmission probability of each spin-polarized channel, is required for assessing the degree of conduction spin-polarization (CSP).

Shot-noise measurements. In molecular junctions[25,26] and generally in a variety of spintronic devices[27–29] the CSP, defined as $P_G = \left| (G_\uparrow - G_\downarrow)/(G_\uparrow + G_\downarrow) \right|$, can be estimated under certain assumptions by magneto-transport measurements in a spin-valve configuration[29]. However, this approach is irrelevant for the studied molecular junction, because such measurements require magnetic electrodes. Instead, we turn to shot-noise measurements that provide useful information about the CSP and the transmission probabilities of spin-polarized channels[30–33]. Electronic shot-noise stems from the discreteness of electrons. When current is transmitted across a quantum conductor, each incident electron can be transmitted with a probability $\tau_{i,\sigma}$ or backscatter with a probability $(1 - \tau_{i,\sigma})$, leading to temporal current fluctuations called shot noise[24]. The relation between shot noise and spin transmission channels for $eV \gg k_B T$ is given by $S = 2eIF$, where I is the current and F is the Fano factor, defined as $F = \sum_{i,\sigma} \tau_{i,\sigma}(1 - \tau_{i,\sigma}) / \sum_{i,\sigma} \tau_{i,\sigma}$. For an arbitrary number of channels i and spin type σ, the CSP depends on the Fano factor as[34] $P_G \geq \left[(2G_0^s(1 - F)/G) - 1 \right]^{1/2}$. Therefore, shot noise provides the lower bound for CSP. Figure 2a presents a plot of Fano factor as a function of conductance space, obtained by solving the above two equations for F and G. In the dark gray area, valid
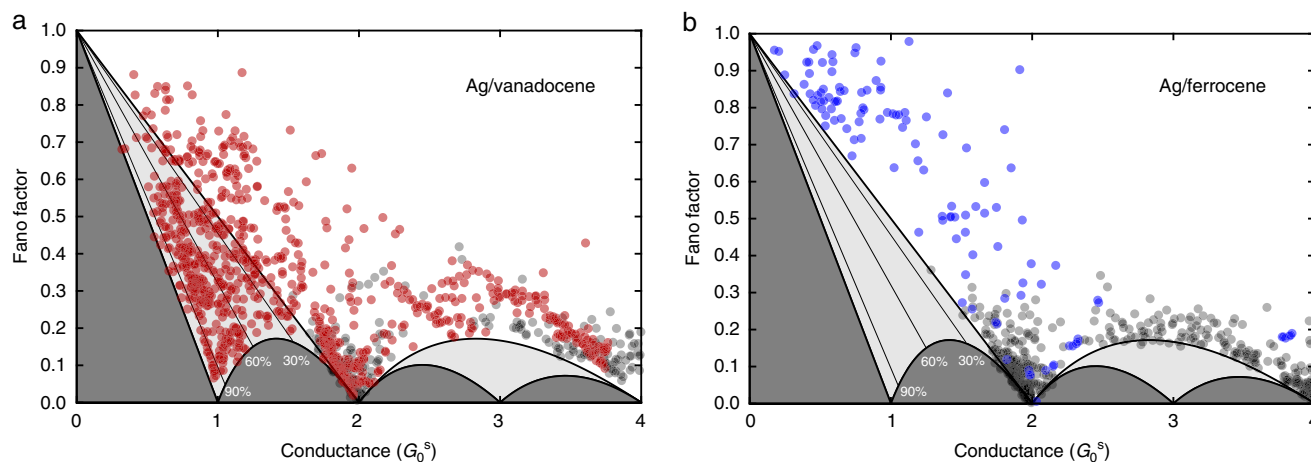

Fig. 2 Fano factor for the studied molecular junctions and the bare silver atomic-scale junctions. **a** Fano factor (F) extracted by shot noise and conductance (G) measurements (see Supplementary Note 2) as a function of conductance for 900 different realizations of Ag/vanadocene molecular junctions (red), and similar measurements for 327 bare silver atomic-scale junctions (black). These data sets were taken independently of the data presented in Fig. 1. **b** The same for 123 Ag/ferrocene molecular junctions (blue), and 1,025 bare silver atomic-scale junctions (black). Data points that are located within the light-gray region imply spin-polarized conductance. The thick black curve separating the light-gray and dark gray areas provides the minimal Fano factor, where data accumulating on this line for a conductance of G_0^s or less indicate junctions with a single spin-polarized transmission channel and $P_G = 100\%$. The thin black lines provide the minimal P_G for data below these lines. (F,G) data obtained for Ag/vanadocene junction clearly penetrate the light-gray region, indicating finite CSP, where for some of these data points $P_G > 90\%$. In contrast, for Ag/ferrocene molecular junctions there is no penetration of data points into the light-gray region. The uncertainty due to systematic errors in our measurements is comparable to or slightly larger than the symbols' diameter, as can be seen in Supplementary Fig. 3.

(F,G) solutions do not exist. Practically, (F,G) data located in this region would indicate an experimental artefact. In the light-gray area, only F and G combinations that lead to finite spin-polarization ($P_G > 0$) can exist[31–33]. The black lines indicate the minimal CSP for data that appear below it. For example, (F,G) data appearing below the line of 30% spin-polarization indicate $P_G > 30\%$ for the measured junction. Finally, data on the border of the dark gray region imply $P_G = 100\%$ (see Supplementary Notes 2 and 3).

In Fig. 2, the data measured for bare silver junctions (black dots) do not penetrate into the light-gray region within the measurement uncertainty (Supplementary Fig. 3), as expected for silver atomic junctions with spin degenerate conductance ($\tau_{i,\uparrow} = \tau_{i,\downarrow}$). Once vanadocene molecules are introduced to form molecular junctions, the distribution of the measured (F,G) data is significantly different, where the large data spread implies a rich set of possible molecular junction structures. Remarkably, a clear penetration to the light-gray region that indicates spin-polarized conductance is observed for many realizations of the Ag/vanadocene junctions. No penetration is observed at high conductance ($G > 2\ G_0^s$), because in these cases the junction is squeezed such that the contact is dominated by Ag atoms. Interestingly, some junctions feature a rather high CSP, as revealed by data below the $P_G = 90\%$ threshold line. While most of the examined junctions exhibit smaller CSP, these cases indicate that some of the molecular junction's geometries act as a very efficient spin-filter.

It is important to stress that the revealed spin filtering in the examined non-magnetic molecular junction has both a concrete fundamental meaning and important practical advantages. From the fundamental point of view, the generated spin-polarized current in the examined non-magnetic system has a well-defined spin orientation in spin space, despite the absence of a defined orientation in the device frame of reference for spin-up and spin down. In this context, there is a fundamental difference between a current of both spin-up and spin down to a current dominated by only one spin type. Focusing on the practical aspects of our

findings, the unique combination of spin filtering in the spin space and an undefined spin orientation with respect to the molecular conductor has interesting advantages. In magnetic systems, the injected spin direction is typically constrained and aligned with the magnetization of the system (e.g., the magnetization of ferromagnetic electrodes). In contrast, the spin current in the presented case has no preference in the device frame of reference. Therefore, it is sufficient to apply a minor magnetic field ($\mathbf{B} > k_B T / \mu$; μ is the magnetic permeability) to orient the spin direction of the spin-polarized current in a desired direction. This ability opens the door to very fast and flexible magnetic manipulations without the limitations imposed by magnetic material properties, including structural changes by magnetostriction, slow hysteretic switching, and power consumption that is translated to unwanted local heating. These advantages can be useful for fast spintronic operations and for the study of dynamical aspects of nanoscale magnetism and spin transport.

To shed light on the relation between our observations and the fact that vanadocene has a finite total spin, we performed control shot-noise measurements on Ag/ferrocene molecular junctions. We chose ferrocene because it has zero total spin and a structure similar to vanadocene, with an iron central atom. Figure 2b presents (F,G) data provided by shot noise and conductance measurements on a set of Ag/ferrocene molecular junctions (see conductance characterization in Supplementary Note 4 and Supplementary Fig. 5). In contrast to the case of Ag/vanadocene, here the (F,G) data do not penetrate into the light-gray area. Thus, for Ag/ferrocene junctions we do not find indications for spin-polarized conductance. These findings suggest that the finite spin of vanadocene plays a role in the generation of spin-polarized conductance.

As seen in Fig. 2a, shot-noise measurements provide indications for relatively highly CSP for some realizations of Ag/vanadocene junctions. The evolution of spin-polarization and the distribution of spin channels for these molecular junctions can be examined during junction elongation. Figure 3 presents two sets
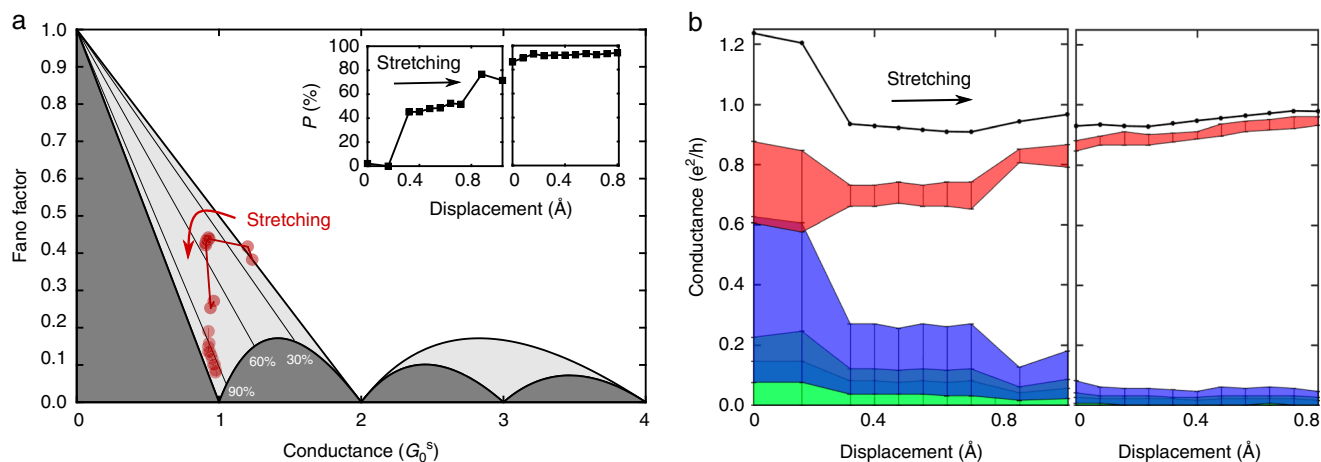

Fig. 3 Experimental analysis of spin-polarized transport during elongation of Ag/vanadocene junctions. **a** Fano factor versus conductance during the elongation of two different Ag/vanadocene junctions. Following each measurement, the junction is stretched by 0.1–0.05 Å. The uncertainty, corresponding to systematic errors in our measurements, is comparable to the symbols' diameter, as shown in Supplementary Fig. 4. Inset, lower bound for CSP (P is the minimal P_G), as determined by the experimentally obtained Fano factor and conductance, with ±3% experimental uncertainty. **b** Total conductance (black dots, error range is given by dots' diameter) and transmission probabilities of the largest four spin-polarized transmission channels (colors). The large uncertainty in the transmission probabilities, indicated by the error bars, stems from the numerical analysis (Supplementary Note 5). As the junction is stretched, the conductance evolves towards the upper limit of ballistic spin-polarized transmission, with conductance approaching G_0^s, spin-polarization approaching 100%, and electron transport that is dominated by a single spin-polarized transmission channel (red-shaded). Here, the maximal values are: $G = 0.98 \pm 0.01\ G_0^s$, $P_G \geq 95 \pm 3\%$, with significant suppression of all spin channels except one. Additional examples for the evolution of transport properties as a function of junction elongation appear in Supplementary Fig. 7. See also Supplementary Note 6.

of (F,G) data as a function of inter-electrode displacement, obtained for two different junction realizations. One set is recorded during the early stages of junction formation, revealing several transmission channels, and a second set shows conductance close to 1 G_0^s dominated by a single transmission channel. During the stretching process, the degree of minimal spin-polarization is increased up to $95 \pm 3\%$ (Fig. 3a, Inset). Figure 3b presents the corresponding evolution of the total conductance (black) and the contribution of each one of the four most dominant spin-polarized channels (colored) to the total conductance. The large uncertainty stems from analyzing numerically the contribution of more than two channels by using only two equations (for shot noise and conductance), as explained in Supplementary Note 5. When the junction has a total conductance of ~1.2 G_0^s, it is carried by several spin-polarized channels. However, as the junction is stretched, most of the channels are suppressed and the conductance is dominated by a single spin-polarized transmission channel, which remains approximately fully-open. These conditions are unique in the sense that they are close to the characteristics of ideal ballistic spin-polarized transport. Namely, conductance of only one spin type with transmission probability of one.

Calculations. To reveal the origin of the observed spin filtering by the Ag/vanadocene junction, we performed calculations of electronic structure and transport based on spin-polarized density-functional theory (DFT) (see Methods). Here, we focus on two junction structures, shown in Fig. 4a, which were found to be stable (see Supplementary Note 7 for structural analysis). Specifically, the perpendicular configuration (left) is more energetically favorable at smaller inter-electrode distances D (defined as the distance between the two Ag apex atoms), while for larger D the parallel configuration (right) is more stable (Supplementary Note 8).

As a first step, we compare the calculated transport properties of these junction structures with our experimental findings. Figure 4b shows spin-resolved total transmissions for two representative perpendicular ($D = 5.8$ Å; minimum total energy; Supplementary Note 9) and parallel ($D = 8.6$ Å) configurations. For the perpendicular configuration, the total transmission (up and down spins) is about 0.96 at the Fermi energy (giving a conductance of 0.96 G_0^s), and is fully spin-polarized. In contrast, the junction with parallel molecular orientation has significantly lower total transmission at the Fermi energy, in the range of 10^{-3} and has very low spin-polarization. Generally, junctions with perpendicular orientation and different inter-electrode separations have a typical total calculated transmission in the range of 0.2–1 at the Fermi energy and a very high spin-polarization (Supplementary Note 9). The agreement of these findings with the experimental indications for spin-polarized conductance in the range of 0.2–1 G_0^s suggest that junctions with perpendicular molecule orientation (Fig. 4a, left) are responsible for the experimentally detected spin-filtering. Supplementary Fig. 6 reveals, on top of significant conductance contribution around 1 G_0^s, lower characteristic conductance with a large spread around 10^{-2}–10^{-3} G_0^s, which can be ascribed to the parallel molecular orientation.

At first sight, the mechanism behind the strong spin filtering found for the perpendicular Ag/vanadocene junctions seems to be rather straightforward. Figure 4c presents the spin-resolved projected density of states (PDOS) on the vanadium d-orbitals, which dominate the molecular states around the Fermi level (for completeness, the pink line in Fig. 4c shows the PDOS on the rest of the molecule). These d-originated states are split due to ligand and magnetic exchange fields, and are mostly

represented at the Fermi energy by the d_{z^2} orbital (Fig. 4c, green lines).

Due to symmetry and spatial orientation, these orbitals hybridize strongly with the silver s-states and therefore provide the main transport channel. Consequently, the spin-dependent transmissions follow very closely their shape (superposing with some sharp features due to other molecular orbitals weakly coupled to the electrodes' states, e.g., at $E = -0.85$ eV for spin-up). Due to rather different spin-up and spin down d_{z^2} PDOS at the Fermi energy, different conductance for each spin type is expected. To quantify the effect, Fig. 4d shows the calculated spin-polarization of d_{z^2} PDOS as a function of energy, defined as $P_{\text{PDOS}}(E) = \left[\text{PDOS}^{\uparrow}(E) - \text{PDOS}^{\downarrow}(E)\right] / \left[\text{PDOS}^{\uparrow}(E) + \text{PDOS}^{\downarrow}(E)\right]$, where $\text{PDOS}^{\sigma}(E)$ is the spin-resolved PDOS for spin-up and down. At the Fermi energy the resulting spin-polarization is only $P_{\text{PDOS}}(E_F) = 67\%$, which is substantial but still not large enough to explain the extreme cases, for example when CSP above 90% is detected by shot-noise measurements (Fig. 2a). Interestingly, previous measurements of transport across cobalt and iron atoms adsorbed between gold electrodes showed limited CSP (30–60%) that is rather typical of a spin-polarized density of state[20]. In contrast, the calculated transmission spin-polarization (Fig. 4d, black curve), defined as $P_T(E) = \left[T^{\uparrow}(E) - T^{\downarrow}(E)\right] / \left[T^{\uparrow}(E) + T^{\downarrow}(E)\right]$ for a total spin-resolved transmission T^{σ}, is nearly -100%, over a wide range of energies around the Fermi energy. Here, minus indicates a dominant spin-down contribution. The calculated $P_T(E_F)$ describes well the experimental indications for high CSP in some of the examined junction configurations. However, our calculations reveal that the high transport spin polarization cannot be escribed to differences in the density of states for opposite spins. We note that further calculations using different methodology (Supplementary Note 8 and Supplementary Fig. 11) provide similar results.

Discussion

In what follows, we present clear indications that the very high spin-polarization found both by experiment and transmission calculations stems from quantum interference between different current pathways across the Ag/vanadocene junction. The signature of interference is seen in the transmission calculations (Fig. 4b) but not in the PDOS calculations (Fig. 4c) because it is an outcome of interfering electronic transport pathways, rather than an outcome of local orbital hybridization. The first hint for interference is the asymmetric shape of the rather broad spin-up transmission peak centered at around $E = -1.2$ eV (Fig. 4b). While the transmission reduction is moderate at $E < -1.2$ eV, it is severely suppressed towards the Fermi energy, where it is negligibly small (0.005), giving rise to essentially $P_T(E_F) \cong 100\%$. In contrast, the PDOS seen in Fig. 4b remains finite, leading to $P_{\text{PDOS}}(E_F) = 67\%$ (Fig. 4d). The interference in transmission is revealed upon considering the contributions of different pathways to the total transmission of the examined junction, seen in Fig. 4e, which can be easily calculated within our tight-binding code by setting appropriate hopping parameters to zero. For spin-up transmission, the individual contributions across the vanadium d_{z^2} level (green) and the π system of the carbon rings (pink) are both significant near the Fermi energy, but the total contribution of the two pathways (black dashed) is clearly lower than their individual contributions. This indicates a destructive interference near the Fermi energy. Additional secondary pathways (e.g., direct tunneling between the electrodes) further contribute to the destructive interference, leading to yet more efficient suppression in the total spin-up transmission (black). The interplay between the different pathways for spin-down is considerably different. In this case, the two main pathways (as well as all pathways)
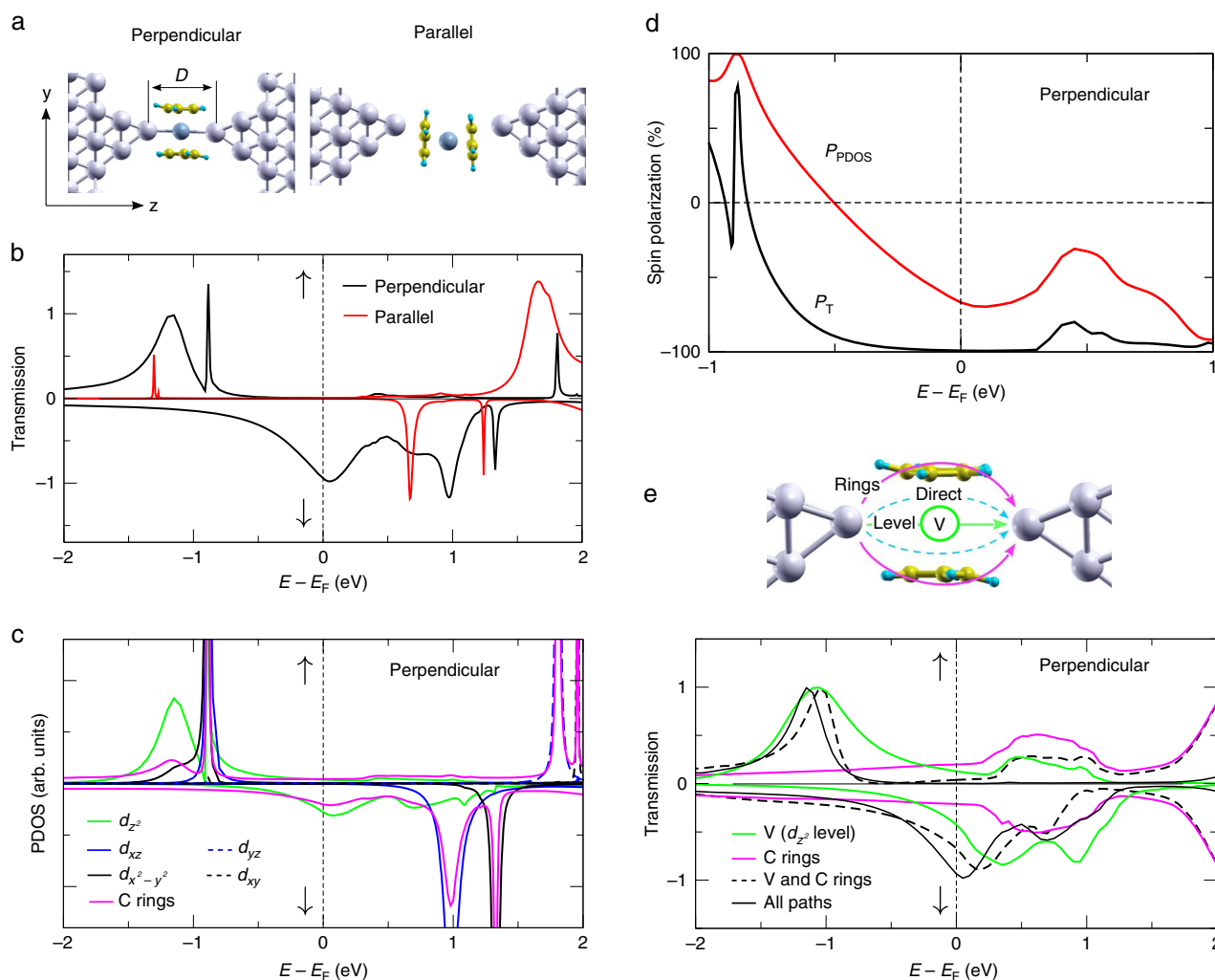
Fig. 4 Calculations for spin-polarized transport across Ag/vanadocene junctions. **a** Two junction configurations characterized by perpendicular (left) and parallel (right) molecular orientation with respect to the junction axis. **b** Spin-resolved transmission versus energy for the two junction configurations. **c** Spin-resolved projected density of states (PDOS) on the vanadium d orbitals for perpendicular molecular configuration (see also Supplementary Note 10). The PDOS on the rest of the molecule (two carbon rings) is shown in pink. The origin for the different widths of the spin-up and down transmission peaks is discussed in Supplementary Note 11. **d** Spin-polarization of transmission and vanadium d_{z^2} PDOS (P_T and P_{PDOS}, respectively) for the perpendicular molecular configuration. Interestingly, P_T remains rather high even at $E < -0.5$ eV, where P_{PDOS} is nullified and even changes its sign. **e** Spin-resolved transmission for different current pathways across the junction in the perpendicular molecular configuration. Two main transmission pathways—across the carbon rings (pink lines) and across the vanadium d_{z^2} level (green lines)—are found to play an essential role interfering destructively (constructively) at the Fermi level for spin-up (down) electrons, as seen by their overall contribution in black dashed lines. The black line describes all contributions (including direct silver-silver tunneling, for example). The origin for the shift in the transmission peaks is discussed in Supplementary Note 12.

contribute constructively at the Fermi energy, summing up to a transmission almost equal to one, and hence to highly spin-polarized conductance close to 1 G_0^s.

The demonstrated spin-dependent quantum interference is essential for having highly spin-polarized conductance in the examined molecular junction. This mechanism stems from an interplay of two main effects, as can be seen in Fig. 4b: an asymmetric shape of the d_{z^2} related transmission peak (as can be clearly observed for spin-up channel around −1.2 eV), reflecting the destructive (constructive) interference to the right (left) of its maximum; and a single occupancy of the highly conductive vanadium d_{z^2} level, which therefore appears below (above) the Fermi energy for spin-up (spin-down) electrons. While the effect of quantum interference on charge transport has been extensively studied experimentally in molecular junctions[11–19], the effect of quantum interference on spin transport has not been demonstrated in such junctions or, generally, at the nanoscale.

Specifically, spin-dependent quantum interference was studied experimentally merely in large systems, such as microscale GaAs and graphene devices[34,35], which are more sensitive to decoherence effects due to their size. The presented spin-dependent quantum interference in molecular junctions can be nicely reproduced by a tight-binding toy model as discussed in Supplementary Note 13, where it is also shown how the resulting transmission line-shapes can be readily rationalized in terms of scattering phase shifts.

To conclude, we experimentally demonstrate that a single-molecule junction can act as an efficient spin-filter without the use of ferromagnetic components. The conductance of the examined Ag/vanadocene molecular junctions approaches in some cases the limit of ideal ballistic spin transport, where it is primarily dominated by a single spin-polarized transmission channel, which is nearly fully open. Such efficient spin filtering in a non-magnetic nanoscale system pave the way to fast and power-

saving spin-current manipulations based on small and dynamic magnetic fields. Based on detailed comparison of ab initio calculations to shot-noise and conductance measurements, we ascribe the efficient spin filtering found for many of the examined junctions to spin-dependent quantum interference. This mechanism is based on the combination of spin-split energy levels near the Fermi energy and quantum interference. Together, they lead to destructive interference for one spin type and constructive interference for the opposite spin type at the Fermi energy. Our findings show that spin-dependent quantum interference can be obtained at the single-molecule level. This mechanism can be used as an efficient scheme for spin filtering at the nanometer down to sub-nanometer scale, with the advantage of lower sensitivity to decoherence effects in these length scales.

Methods

Experiments. Our experiments were conducted in a mechanically controllable break-junction[11] setup (MCBJ) placed in a liquid helium cryostat. A silver wire (99.997%, 0.1 mm, Alfa Aesar) with a notch in its center is attached to a flexible substrate (1-mm-thick phosphor-bronze covered by 100 μm insulating Kapton film). This structure is placed in a cryogenic insert, which is pumped to 10^{-4} mbar and then cooled down to 4.2 K by dipping it in the cryostat. A three-point bending mechanism is used to bend the substrate (Fig. 1b). Consequentially, the wire is broken at the notch, exposing (in cryogenic vacuum) two ultra-clean atomically sharp tips that are used as the junction's electrodes. A piezoelectric element (PI P-882 PICMA) is used to tune the bending of the substrate and control the inter-electrode distance with sub-Å resolution. This element is driven by a 24-bit NI-PCI4461 data acquisition (DAQ) card, followed by a Piezomechanik SVR 150/1 piezo driver. An ensemble of junctions with diverse structures is studied by repeatedly pushing the electrodes together to form a contact of ~100–140 G_0^s and pulling the electrodes apart until full rupture. The vanadocene or ferrocene molecules (95%, Stream Chemicals and 99.5%, Alpha Aesar, respectively, further purified in situ) are introduced into the metallic junction by sublimation from a locally heated molecular source towards the repeatedly broken and reformed junction[12]. In order to measure the conductance traces, direct-current (d.c.) conductance is probed, when the junction is gradually broken by increasing the applied voltage on the piezoelectric element at a speed of 600 nm s^{-1} and a 100 kHz sampling rate. A constant voltage of 10–200 mV is applied across the junction by a NI-PCI4461 DAQ card. The generated current is amplified by a current pre-amplifier (Femto DLPCA-200) and recorded by the DAQ card. The obtained conductance is given by the measured current divided by the applied voltage. The inter-electrode displacement is estimated by the dependence of tunneling current on the distance between the electrodes. Measurements of differential conductance (dI/dV versus V; e.g., Supplementary Fig. 2) are performed using a standard lock-in technique. A reference sine signal of 1 mV peak-to-peak voltage (Vpp) at ~3 kHz, modulating a d.c. bias voltage is supplied by the DAQ card. The alternating-current (a.c.) response is recorded by the DAQ card and extracted by either a LabView implemented lock-in or a SR830 lock-in to obtain the differential conductance as a function of applied voltage. Noise measurement are performed when the instruments used for conductance measurements are disconnected from the sample to reduce extrinsic noise. The voltage noise generated in the junction is amplified by a custom-made differential low-noise amplifier, which is calibrated by the thermal noise of a set of known resistors located in liquid nitrogen. A power spectrum between 0.25 kHz and 300 kHz is measured via the NI-PXI5922 DAQ card, using a LabView implemented fast Fourier transform analysis and averaged 3,000 times. To probe shot noise, the sample is biased by current, using a voltage source (NI-PCI4461 DAQ card) connected to the sample through two 2 MΩ resistors located near the sample (the resistors convert the voltage bias into current bias). All amplifiers are powered by batteries to avoid the injection of unwanted noise from power lines.

Calculations. Spin-polarized density-functional theory (DFT) calculations shown in Fig. 4 were performed using planewaves and ultrasoft pseudopotentials, as implemented in the Quantum-ESPRESSO (QE)[36] package. The Perdew-Burke-Ernzerhof (PBE)[37] exchange-correlation functional was used throughout. The molecular junctions shown in Fig. 4 were described by a supercell containing the molecule and two 4-atom Ag pyramids attached to a Ag(111) slab containing five and four atomic layers on the left and right side, respectively. A 4 × 4 in plane periodicity (16 atoms per Ag layer) was employed to avoid artificial molecule/molecule interactions. Spin-polarized transport was studied using a home-made tight-binding code[38] with tight-binding parameters extracted from the first principles QE calculations. The standard non-equilibrium Green's function (NEGF) formalism was employed to compute spin-dependent transmission functions, defining the coherent conductance in the framework of the Landauer-Büttiker formalism.

The calculations presented in Supplementary Fig. 10 and 11 were performed as follows. The molecular geometry of the junction was the same as in the above

calculations. Electronic structure calculations were carried out using density-functional theory (DFT) as implemented in the SIESTA[39] and VASP[40] codes, with the PBE exchange-correlation functional. Geometrical optimization was performed using VASP and the optimized geometries were used in the SIESTA calculations. Spin-dependent electron transport calculations were performed using the TRANSIESTA[41] code, which performs a non-equilibrium Green's-function (NEGF) calculation based on the DFT results.

References

1. Giovannetti, V., Lloyd, S. & Maccone, L. Quantum metrology. *Phys. Rev. Lett.* **96**, 010401 (2006).
2. Nielsen, M. A. & Chuang, I. *Quantum computation and quantum information* 10th edn. (Cambridge University Press, 2010).
3. Brumer, P. & Shapiro, M. Coherence chemistry: controlling chemical reactions [with lasers]. *Acc. Chem. Res.* **22**, 407–413 (1989).
4. Solomon, G. C., Andrews, D. Q., Van Duyne, R. P. & Ratner, M. A. When things are not as they seem: quantum interference turns molecular electron transfer "rules" upside down. *J. Am. Chem. Soc.* **130**, 7788–7789 (2008).
5. Sautet, P. & Joachim, C. Electronic interference produced by a benzene embedded in a polyacetylene chain. *Chem. Phys. Lett.* **153**, 511–516 (1988).
6. Baer, R. & Neuhauser, Phase coherent electronics: a molecular switch based on quantum interference. *J. Am. Chem. Soc.* **124**, 4200–4201 (2002).
7. Stafford, C. A., Cardamone, D. M. & Mazumdar, S. The quantum interference effect transistor. *Nanotechnology* **18**, 424014 (2007).
8. Andrews, D. Q., Solomon, G. C., Van Duyne, R. P. & Ratner, M. A. Single molecule electronics: increasing dynamic range and switching speed using cross-conjugated species. *J. Am. Chem. Soc.* **130**, 17309–17319 (2008).
9. Rai, D., Hod, O. & Nitzan, A. Circular currents in molecular wires. *J. Phys. Chem. C* **114**, 20583–20594 (2010).
10. Markussen, T., Stadler, R. & Thygesen, K. S. The relation between structure and quantum interference in single molecule junctions. *Nano Lett.* **10**, 4260 (2010).
11. Guédon, C. M. et al. Observation of quantum interference in molecular charge transport. *Nat. Nanotechnol.* **7**, 305–309 (2012).
12. Darwish, N. et al. Observation of Electrochemically Controlled Quantum Interference in a Single Anthraquinone-Based Norbornylogous Bridge Molecule. *Angew. Chem. Int. Ed.* **51**, 3203–3206 (2012).
13. Aradhya, S. V. et al. Dissecting contact mechanics from quantum interference in single-molecule junctions of stilbene derivatives. *Nano Lett.* **12**, 1643–1647 (2012).
14. Ballmann, S. et al. Experimental evidence for quantum interference and vibrationally induced decoherence in single-molecule junctions. *Phys. Rev. Lett.* **109**, 056801 (2012).
15. Frisenda, R., Janssen, V., Grozema, F., van der Zant, H. & Renaud, N. Mechanically controlled quantum interference in individual π-stacked dimers. *Nat. Chem.* **8**, 1099–1104 (2016).
16. Garner, M. H. et al. Comprehensive suppression of single-molecule conductance using destructive σ-interference. *Nature* **558**, 415–419 (2018).
17. Li, Y. et al. Gate controlling of quantum interference and direct observation of anti-resonances in single molecule charge transport. *Nat. Mater.* **4**, 357–363 (2019).
18. Bai, J. et al. Anti-resonance features of destructive quantum interference in single-molecule thiophene junctions achieved by electrochemical gating. *Nat. Mater.* **4**, 364–369 (2019).
19. Vázquez, H. et al. Probing the conductance superposition law in single-molecule circuits with parallel paths. *Nat. Nanotech.* **7**, 663 (2012).
20. Jackson, T. A. et al. Vanadocene de novo: spectroscopic and computational analysis of bis (η5 cyclopentadienyl) vanadium (II). *Organometallics* **31**, 8265–8274 (2012). **10**.
21. Agraït, N., Yeyati, A. L. & van Ruitenbeek, J. M. Quantum properties of atomic-sized conductors. *Phys. Rep.* **377**, 81–279 (2003).
22. Yelin, T. et al. Conductance saturation in a series of highly transmitting molecular junctions. *Nat. Mater.* **15**, 444–449 (2016).
23. Nath Pal, A., Klein, T., Vilan, A. & Tal, O. Electronic conduction during the formation stages of a single-molecule junction. *Beilstein J. Nanotech.* **9**, 1471–1477 (2018).
24. Blanter, Y. M. & Büttiker, M. Shot noise in mesoscopic conductors. *Phys. Rep.* **336**, 1–66 (2000).

25. Schmaus, S. et al. Giant magnetoresistance through a single molecule. *Nat. Nanotech.* **6**, 185–189 (2011).
26. Kawahara, S. L. et al. Large magnetoresistance through a single molecule due to a spin-split hybridized orbital. *Nano Lett.* **12**, 4558–4563 (2012).
27. Moodera, J. S., Kinder, L. R., Wong, T. M. & Meservey, R. Large magnetoresistance at room temperature in ferromagnetic thin film tunnel junctions. *Phys. Rev. Lett.* **74**, 3273–3276 (1995).
28. Gurram, M., Omar, S. & van Wees, B. J. Bias induced up to 100% spin-injection and detection polarizations in ferromagnet/bilayer-hBN/graphene/hBN heterostructures. *Nat. Commun.* **8**, 248 (2017).
29. Zutic, I., Fabian, J. & Das Sarma, S. Spintronics: fundamentals and applications. *Rev. Mod. Phys.* **76**, 323–410 (2004).
30. Roche, P. et al. Fano factor reduction on the 0.7 conductance structure of a ballistic one-dimensional wire. *Phys. Rev. Lett.* **93**, 116602 (2004).
31. Kumar, M. et al. Shot noise and magnetism of Pt atomic chains: accumulation of points at the boundary. *Phys. Rev. B* **88**, 245431 (2013).
32. Burtzlaff, A., Weismann, A., Brandbyge, M. & Berndt, R. Shot noise as a probe of spin-polarized transport through single atoms. *Phys. Rev. Lett.* **114**, 016602 (2015).
33. Vardimon, R., Klionsky, M. & Tal, O. Indication of complete spin-filtering in atomic-scale nickel oxide. *Nano Lett.* **15**, 3894–3898 (2015).
34. Folk, J. A., Potok, R. M., Marcus, C. M. & Umansky, V. A gate-controlled bidirectional spin-filter using quantum coherence. *Science* **299**, 679–682 (2003).
35. Lundeberg, M. B. & Folk, J. A. Spin-resolved quantum interference in graphene. *Nat. Phys.* **5**, 894–897 (2009).
36. Paolo, Giannozzi et al. QUANTUM ESPRESSO: a modular and open-source software project for quantum simulations of materials. *J. Phys. Condens. Matter* **21**, 395502 (2009).
37. Perdew, J. P., Burke, K. & Ernzerhof, M. Generalized gradient approximation made simple. *Phys. Rev. Lett.* **77**, 3865 (1996).
38. Autès, G., Barreteau, C., Spanjaard, D. & Desjonquères., M.-C. Electronic transport in iron atomic contacts: from the infinite wire to realistic geometries. *Phys. Rev. B* **77**, 155437 (2008).
39. Soler, J. M. et al. The SIESTA method for ab initio order-N materials simulation. *J. Phys. Condens. Matter* **14**, 2745–22779 (2002).
40. Kresse, G. & Furthmüller, J. Efficient iterative schemes for ab initio total-energy calculations using a plane-wave basis set. *Phys. Rev. B* **54**, 11169 (1996).
41. Brandbyge, M., Mozos, J. L., Ordejón, P., Taylor, J. & Stokbro, K. Density-functional method for nonequilibrium electron transport. *Phys. Rev. B* **65**, 165401 (2002).

Acknowledgements

Author contributions

A.N.P. performed conductance and shot-noise experiments and analysis. S.C. performed conductance experiments and analysis. A.V. carried out conductance analysis. The mentioned experimental work was carried out under the guidance of O.T., D.L. and A.S. performed spin-polarized DFT calculations (QE), as well as tight-binding and model transport simulations. S.S. and L.K. carried out spin-polarized DFT calculations (SIESTA, VASP) and transport calculations (TRANSIESTA). All the authors participated in discussions and co-wrote the paper.

Competing interests

The authors declare no competing interests.

Additional information

Supplementary information is available for this paper at https://doi.org/10.1038/s41467-019-13537-z.

Correspondence and requests for materials should be addressed to O.T.

Peer review information *Nature Communications* thanks the anonymous reviewer(s) for their contribution to the peer review of this work.

Reprints and permission information is available at http://www.nature.com/reprints

Publisher's note Springer Nature remains neutral with regard to jurisdictional claims in published maps and institutional affiliations.
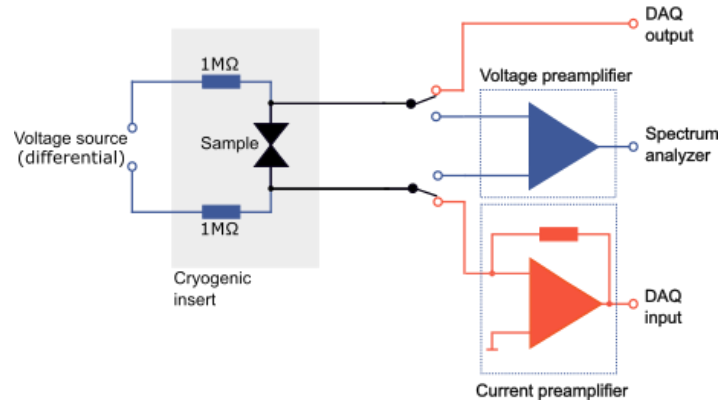
SUPPLEMENTARY INFORMATION

Nonmagnetic single-molecule spin-filter based on quantum interference

Pal *et al.*

Supplementary Note 1.

Electronic measurement circuit

Supplementary Fig. 1 shows the electronic setup connected to the sample. The circuit can be switched between a Conductance Mode, which is used to measure d.c. conductance as well as a.c. (differential) conductance spectra, and a Noise Mode, in which thermal noise and shot noise are measured. In the latter mode of measurement, the relatively noisy instruments used in the conductance mode are disconnected from the sample because of the high sensitivity of the noise measurements.

Supplementary Figure 1. Electronic circuit of the measurement setup. Schematic presentation of the electronic circuit for conductance and noise measurements. Two switchable measurement circuits are observed: a conductance circuit (orange) and a noise circuit (blue). The section cooled to 4.2 K is marked in light gray.

Supplementary Note 2.

Shot noise measurements

The overall zero-frequency current noise (both thermal and shot noises) generated in a quantum coherent conductor can be expressed in the framework of Landauer formalism as[1,2]
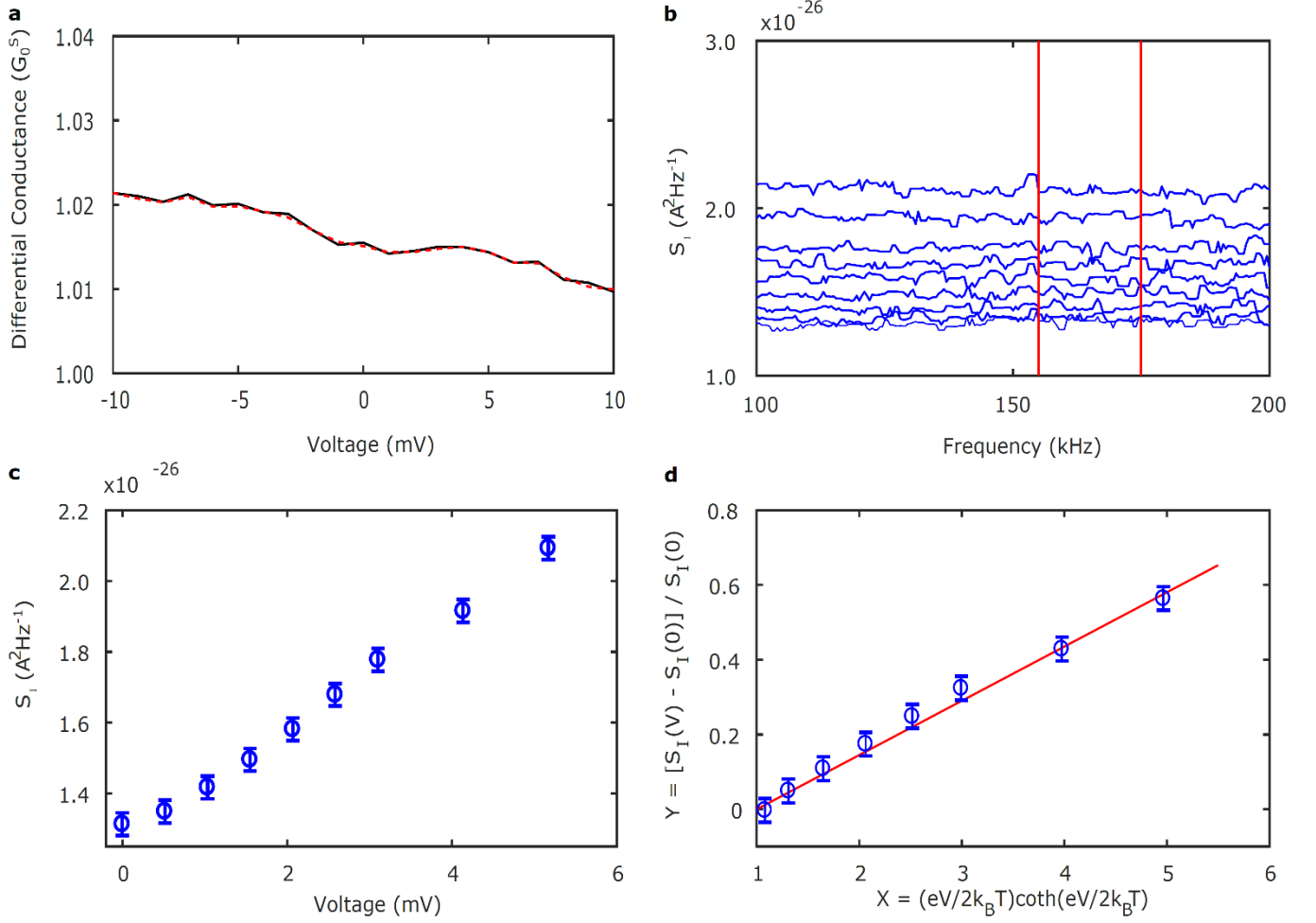
$$S_I = 4k_\mathrm{B}TG[1 + F(x\coth(x) - 1)], \qquad (1)$$

where $x = eV/2k_\mathrm{B}T$ provides the ratio between an applied voltage V and temperature T. At near-equilibrium conditions ($x \ll 1$), equation (1) reduces to the thermal noise expression[1] $S_I = 4k_\mathrm{B}TG$. At high applied voltage ($x \gg 1$), the current noise depends linearly on the current, $S_I = 2eIF$. Supplementary Fig. 2 presents an example of shot noise analysis in an Ag/vanadocene molecular junction. Before and after each set of noise measurements as a function of bias voltage, differential conductance spectra (dI/dV versus V; Supplementary Fig. 2a), are recorded in order to confirm that the junction has remained stable during the noise measurements. The zero-bias conductance of the junction is determined from the average differential conductance in a window of $|V| \leq 5\,mV$. Variations in the conductance at this range are taken into consideration as an experimental error.

Supplementary Fig. 2b presents a set of noise spectra for different applied current. Note that the bias current produces bias voltage across the junction ($V = I/G$). Each spectrum is obtained from the Fourier transform of voltage fluctuations produced by the junction, and averaged for 3,000 consecutive measurements. The voltage noise produced by the amplifier was measured separately and subtracted from the recorded spectra. The measured voltage noise is presented as a current noise using the relation $S_I = S_V \cdot G^2$. Next, the spectra were corrected to account for low-pass RC filtering due to the resistance of the sample and cabling, as well as the amplifier input capacitance and the capacitance of the cabling (total capacitance of $\sim 40\,pF$). The noise power is averaged in a frequency window, in which $1/f$ noise contributions are negligible (marked by red lined in Supplementary Fig. 2b). Supplementary Fig. 2c shows the obtained average current noise power as a function of the generated bias voltage across the junction. Following Ref. 2, Eq. (1) can be expressed as

$$Y = F(X - 1). \qquad\qquad (2)$$

Here, $X = x coth(x)$ and $Y = [S_I(V) - S_I(0)]/S_I(0)$. The Fano factor is obtained by calculating the reduced parameters X and Y and obtaining a linear fit of $Y(X)$ according to Eq. (2), as shown in Supplementary Fig. 2d. Occasionally, we observed zero-bias anomalies in the differential conductance curves that may originate from different possible mechanisms, including Kondo physics. The data obtained in these specific cases will be analyzed and reported elsewhere, since the physics involved is beyond the Landauer formalism considered here.

Supplementary Figure 2: Analysis of shot noise measured in an Ag/vanadocene junction. a, Differential conductance versus voltage curves measured for an Ag/vanadocene junction before (black) and after (dashed red) noise measurements. **b,** A series of current noise spectra for different bias voltage across the junction. Red lines indicate the frequency window that is selected to obtain the average noise power. **c,** Average current noise power as function of bias voltage calculated using the presented noise in (b). **d,** Reduced parameter Y as a function of X (blue) calculated using the measured noise in (c), and a linear fit (red), giving $F = 0.15 \pm 0.01$ according to Supplementary Eq. (2).
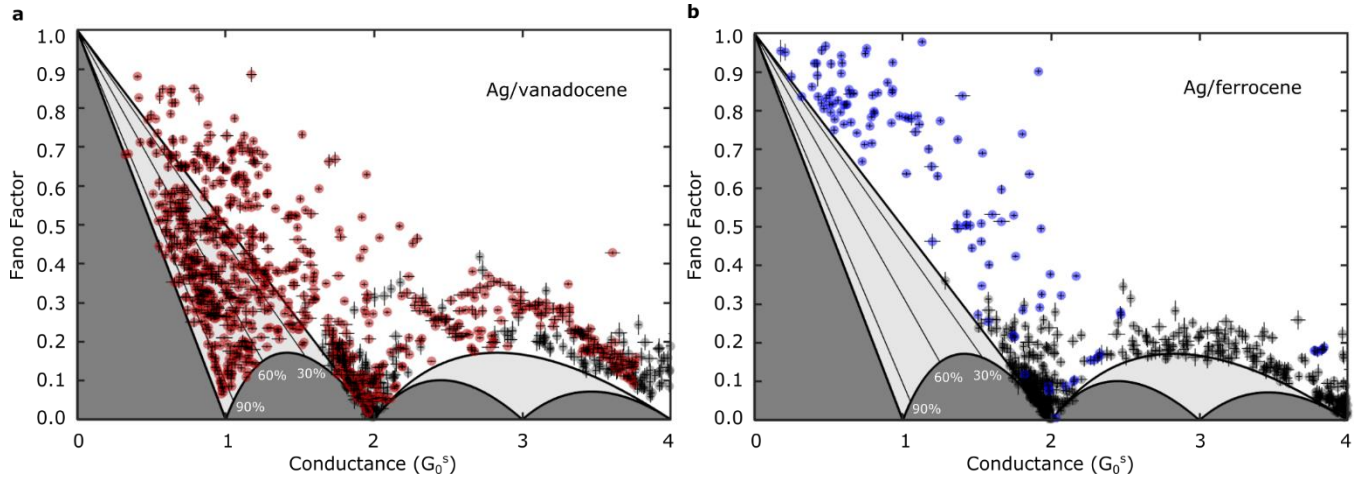
Supplementary Note 3.

Determination of conductance spin polarization by shot noise measurements

Shot noise measurements were used in a variety of nanoscale and mesoscopic systems to gain information on spin transport effects[2-7]. In a quantum coherent conductor with an unknown number of transmission channels, the combination of conductance and shot noise measurements provides a lower bound for the degree of conductance spin polarization (CSP)[6]. In the following, we wish to elaborate on the meaning of the (F, G) plot presented in Fig. 2 and the information that can be derived from this plot. In the Landauer framework, shot
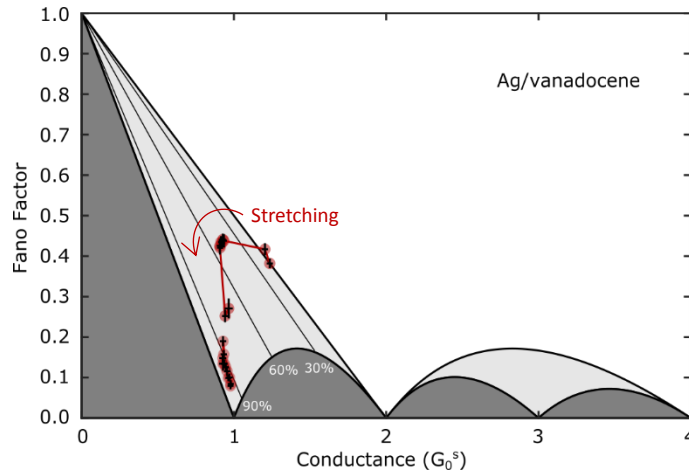
noise depends on $\sum_{i,\sigma} \tau_{i,\sigma}(1 - \tau_{i,\sigma})$, whereas the conductance depends on $\sum_{i,\sigma} \tau_{i,\sigma}$. The (F, G) plot illustrates this dependence.

For zero spin-polarization, the conductance is carried by one or more pairs of spin-polarized transmission channels for opposite spins with equal transmissions ($\tau_{1,\uparrow} = \tau_{1,\downarrow}, \tau_{2,\uparrow} = \tau_{2,\downarrow}, \dots$). For example, the conductance of a single-atom junction of silver is carried by two equal and opposite spin-polarized transmission channels that are associated with the single *s* valence orbital of silver. For zero CSP, the (F, G) data points can have any value in the white region of Fig. 2 in the main text. However, the dark and light gray regions are forbidden. For finite spin-polarization, the constraint $\tau_{i,\uparrow} = \tau_{i,\downarrow}$ does not hold and the forbidden region (presented now in dark gray) is "squeezed" by a factor of 2 along the conductance axis. As a result, any (F, G) combination that is located in the light gray region indicates a finite spin-polarization.

A lower bound for the CSP can be given by the following analysis. Assuming only two spin-polarized channels of opposite spin type, the Fano factor can be rewritten in terms of $P_G^{2\text{ch}}$ (P_G is defined in the main text, and P_G^{2ch} is P_G for two channels) as follows: $F = 1 - G(1 + (P_G^{2\text{ch}})^2)/2G_0^s$, and hence $P_G^{2\text{ch}} = [2G_0^s/(1 - F)/G - 1]^{1/2}$. In contrast, for two spin-polarized channels of the same spin type, the CSP is 100%. Since shot noise does not provide information about the spin type, for two spin channels of an unknown spin type the CSP is either $P_G^{2\text{ch}}$ or 100%. According to the derivation that appears in the Supplementary Information of Ref. 6, for any number of spin-polarized transmission channels $P_G \geq P_G^{2\text{ch}}$ holds. As a result, shot noise measurements (accompanied with conductance measurements) provide the lower bound of CSP for an arbitrary number of spin-polarized transmission channels. In the special case of conductance carried by a single spin-polarized transmission channel, (F, G) data are located on the border of the dark gray region in Fig. 2 (thick black line), where P_G = 100%.

Supplementary Figure 3: Fano Factor for bare silver atomic scale junctions, Ag/vanadocene (*S*=3/2) and Ag/ferrocene (*S*=0) molecular junctions. Fano factor (F) extracted from shot noise and conductance measurements on the examined junctions as a function of conductance (G), as presented in Fig. 2a, b, including error bars, corresponding to the systematic errors in our measurements. The size of the error bars is comparable to or slightly larger than the diameter of the semitransparent symbols.
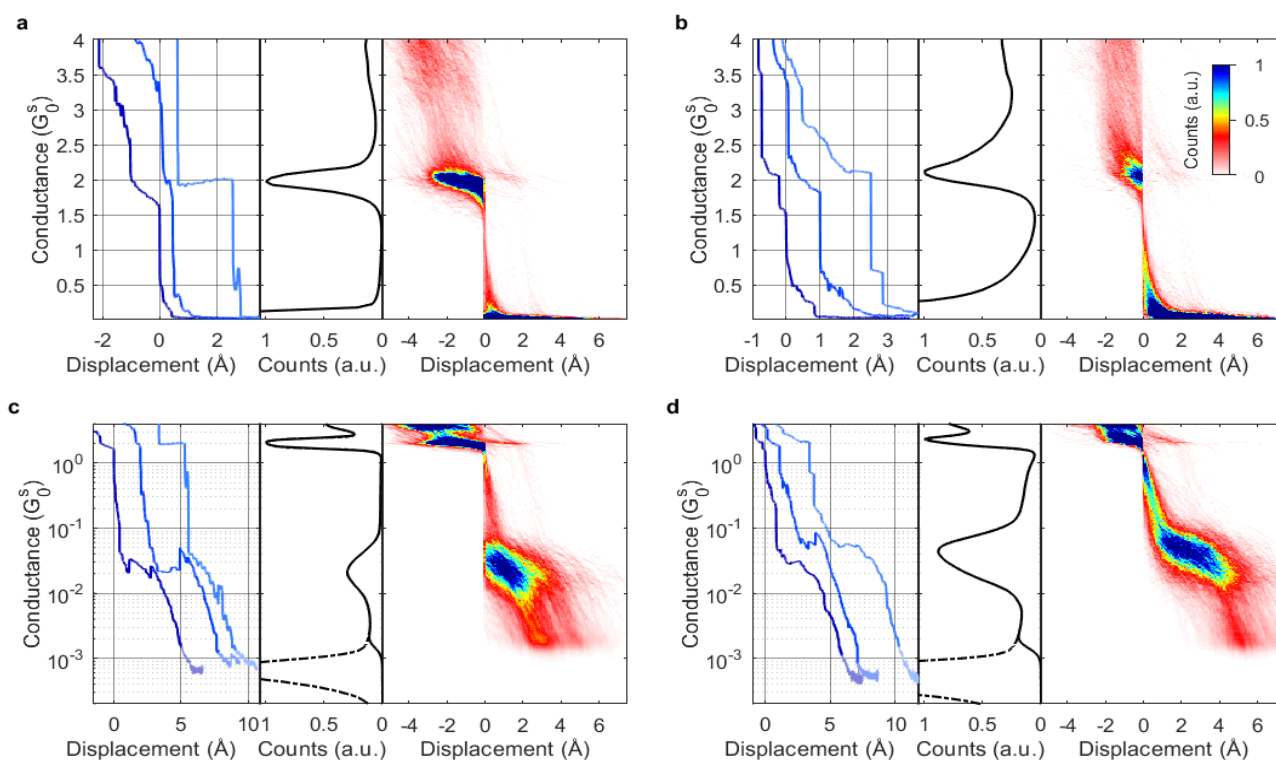

Supplementary Figure 4: Fano Factor during elongation of Ag/vanadocene molecular junctions. Fano factor extracted from shot noise and conductance measurements of the examined junctions versus conductance, during the elongation of the junctions as presented in Fig. 3a, including error bars. The error bars correspond to systematic errors in our measurements. The size of the error bars is comparable to the diameter of the semitransparent symbols.
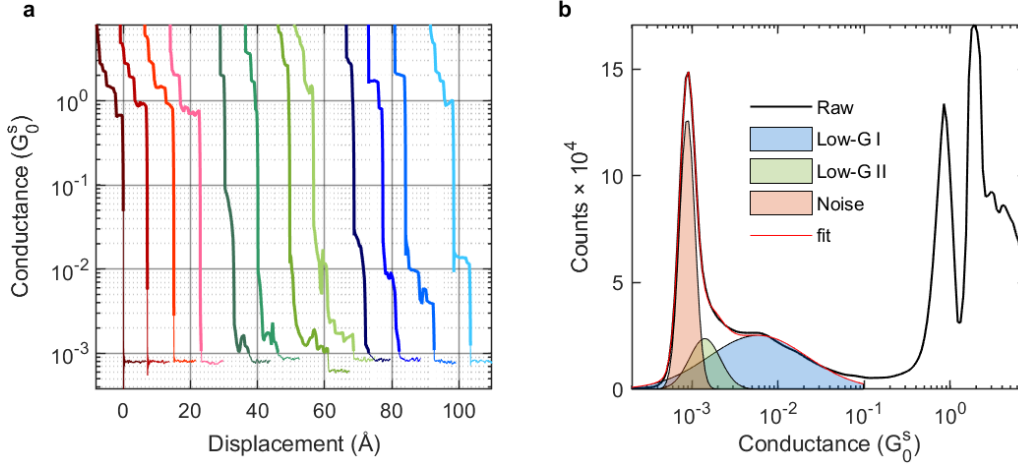
Supplementary Note 4.

Conductance measurements of Ag/ferrocene and Ag/vanadocene molecular junctions

In Supplementary Fig. 5a,b, left panels, plateaus and tilted plateaus below the peak of 2 G_0^s and above 0.1 G_0^s can be observed. These conductance values are repeatable despite the fact that $2\text{-}5 \cdot 10^{-2}$ G_0^s is the most probable conductance of Ag/ferrocene junctions as seen in Supplementary Fig. 5c,d, middle panels. Based on comparison of the conductance histograms in Supplementary Fig. 5a,b, middle panels, it is clear that the contribution of these plateaus to the histogram is higher during the formation process (Supplementary Fig. 5b; i.e., they are more abundant during this process). In view of these observations, the shot noise measurements that are performed on Ag/ferrocene junctions and presented in Fig. 2b were taken on junctions with different fixed inter electrode distance, following a formation process. During this procedure, the opposite electrodes are brought together until a contact is formed. Repeating this procedure provides shot noise measurements of different junction configurations characterized by different conductance.

Supplementary Figure 5: Conductance of Ag/ferrocene molecular junctions. Characterization of Ag/ferrocene molecular junctions, where the data are presented in a linear (a,b) and a logarithmic (c,d) conductance scale, with data measured during junction breaking (a,c) and reformation (b,d). In each figure: **Left panel**, examples for conductance versus inter-electrode displacement traces. Traces are shifted in the displacement axis for clarity. **Middle panel**, conductance histogram constructed from 2,000 conductance traces recorded at a bias voltage of 100 mV. **Right panel**, conductance–displacement density plot based on the same conductance traces. Zero displacement is set for each trace as the first displacement point with a conductance below 4 G_0^s.

Supplementary Figure 6: Conductance of Ag/vanadocene molecular junctions. a, Examples for conductance as a function of inter-electrode displacement traces, recorded at a bias voltage of 100 mV. The traces are shifted in the displacement axis for clarity. Here, the plateau around 1 G_0^s is sometimes followed by another plateau with a lower conductance around 10^{-2}-10^{-3} G_0^s, at larger inter-electrode distances. **b,** Conductance histogram constructed from more than 2,000 traces. The histogram can be fitted (red curve) at conductance below 10^{-1} G_0^s to three Gaussians. The red Gaussian describes the amplifier noise floor and the others reveal two main conductance distributions, centered at $6 \cdot 10^{-2}$ G_0^s (Low-G I; blue Gaussian) and $1.4 \cdot 10^{-3}$ G_0^s (Low-G II; green Gaussian). Examples for the traces that construct each Gaussian are given in (a), using a color code.
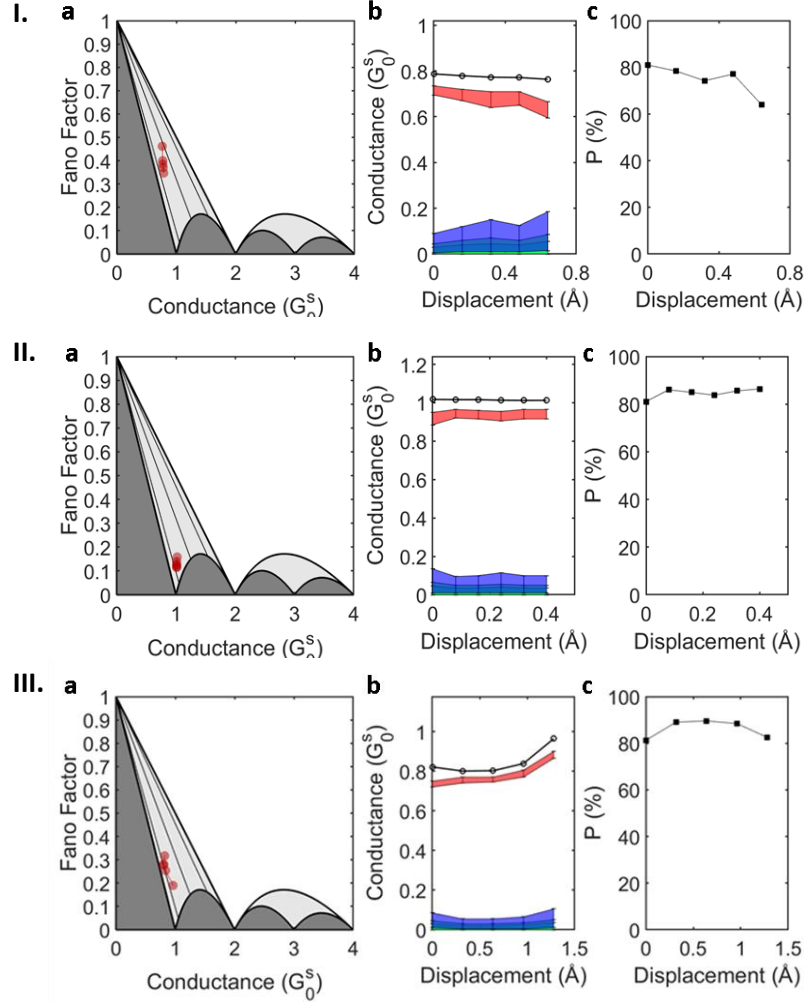
Supplementary Note 5.

Numerical analysis of transmission channel distributions

We briefly describe the numerical procedure used to determine the channel distribution in Fig. 3b in the main text. The full derivation can be found in Ref. 8. A combination of F and G extracted from shot noise and conductance measurements can result from an infinite number of possible combinations of transmission probabilities, $\tau_{i,\sigma}$. However, one can limit the number of possible transmission sets to a finite number by using a finite precision $\Delta\tau$ for the transmission probabilities. For a given number of transmission channels 2N (N channels of each spin type), our procedure enumerates the $2N/\Delta\tau$ possible sets of transmission probabilities, $\{\tau_{i,\sigma}\}_{i=1}^{N}$. We can set the coefficients to be ordered by decreasing transmission: $\tau_{1,\sigma} \geq \tau_{2,\sigma} \geq \cdots \tau_{N,\sigma}$. Note that the difference between adjacent transmission coefficients is $\Delta\tau$. For each set, the Fano factor and conductance are computed and compared to the experimental values of F and G. A set of transmission probabilities is considered to match the experimentally based (F, G) values if it satisfies the following inequalities:

$$G - \Delta G \leq G_0^s \sum_{\sigma,i=1}^{i=N} \tau_{i,\sigma} \leq G + \Delta G, \qquad (3)$$

$$F - \Delta F \leq \sum_{\sigma,i=1}^{i=N} \tau_{i,\sigma}(1 - \tau_{i,\sigma}) \Big/ \sum_{\sigma,i=1}^{i=N} \tau_{i,\sigma} \leq F + \Delta F, \qquad (4)$$

8

where ΔG and ΔF are the experimental errors in G and F, respectively. We define $\{\tau_{j,i,\sigma}\}_{i=1}^{N}$ as the jth set out of k transmission sets that match the experimental values. The transmission coefficient $\tau_{i,\sigma}$ can now be determined to be in the range between $\tau_{j,i,\sigma}^{\min} = \min\{\tau_{i,\sigma}\}_{j=1}^{k} - \Delta\tau$ and $\tau_{j,i,\sigma}^{\max} = max\{\tau_{i,\sigma}\}_{j=1}^{k} + \Delta\tau$. Here, $\Delta\tau$ are added to certify that all possible solutions for $\tau_{i,\sigma}$ are included in this range. In this analysis, we assume *a priori* a given number of channels. However, we can repeat the procedure for *N+1*, *N+2*,… to obtain convergence of the channel distribution. This procedure helps us avoid a deficient estimation of N.

Supplementary Figure 7: Experimental analysis of spin-polarized transport during elongation of Ag\vanadocene junctions, as in Fig. 3 in the main text. **a,** Fano factor versus conductance during the elongation of three different Ag\vanadocene junctions. Following each measurement, the junction is stretched by up to 0.25 Å. The uncertainty, corresponding to systematic errors in our measurements, is comparable to the diameter of the semitransparent symbols, as shown in Supplementary Fig. 3 and 4. **b**, Total conductance (black dots, error range is given by dots' diameter) and transmission probabilities of the largest four spin-polarized transmission channels (colors). The large uncertainty in the channel transmissions stems from the numerical analysis (Supplementary Note 5). **c**, lower bound for CSP (P is the minimal P_G), as determined by the experimentally obtained Fano factor and conductance, with ± 3% experimental uncertainty. The different panels exemplify reduction (I), insensitivity (II), and non-monotonic (III) CSP response to junction stretching.

Supplementary Note 6.

Experimental analysis of spin-polarized transport during elongation of Ag/vanadocene junctions

The goal of Fig. 3 in the main text is to show that in some cases the conductance can approach the limit of ideal spin polarized ballistic conductance. The limit is given by a single fully open spin polarized transmission channel, namely $G=e^2/h$, $F=0$. As a result, we focus in Fig. 3, main text on stretching sequences, approaching this limit. Examining the entire measured data of transport vs. stretching, including cases that do not approach the spin-transport ballistic limit, we find that the CSP can evolve in different ways in response to junction elongation. This is actually expected considering the non-monotonic evolution of spin polarization as a function of inter-electrode distance as revealed by the different DFT and transport calculations presented in Supplementary Fig. 11 and 12. Over all, we examined 43 shot noise vs. junction elongation traces (see some example in Supplementary Fig. 7) and found 11 traces with increased CSP, 8 traces with decreased CSP, 16 traces with a non-monotonic behavior, and 8 traces with CSP rather insensitive to stretching. Since not always a single trace can capture the entire non-monotonic behavior, these results are in line with the outcome of our calculations.

Supplementary Note 7.

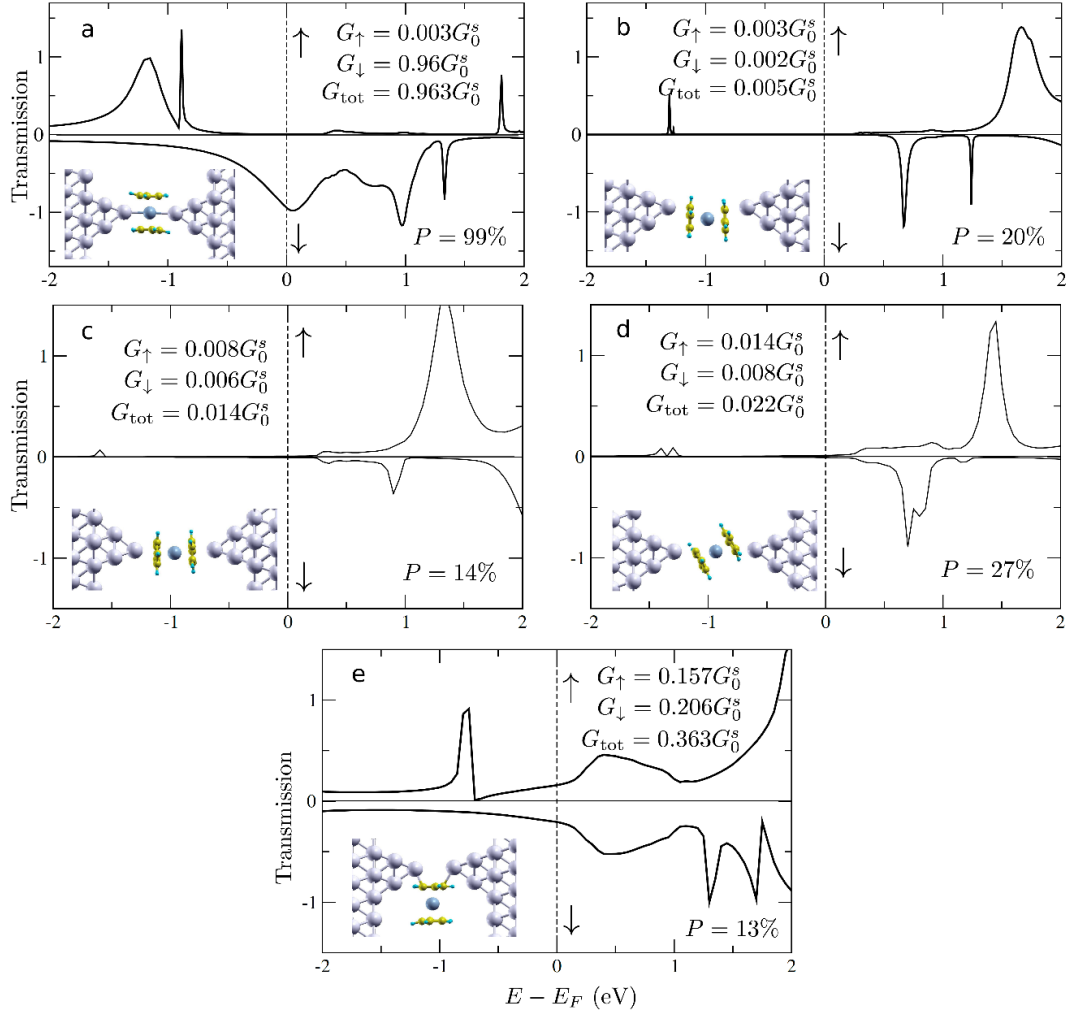**Structural analysis based on DFT and transport calculations**

The connection of the vanadocene molecule to the electrodes is based on chemical binding (see further analysis of the total binding energy in Supplementary Note 9). Therefore, the number of stable junction configurations is limited to molecular orientations that allow such binding, and can be classified into several archetypical configurations. The classification describes the different symmetries possible for the chemical binding between the molecule and the electrodes.

Supplementary Figure 8 presents five different architypes of molecular junction configurations, with different chemical binding sites. For convenience, we also present the perpendicular (in-axis) and parallel (off-axis) molecular orientation (Supplementary Fig. 8a,b) considered in the main text, and we add the following configurations: parallel in-axis (Supplementary Fig. 8c), tilted (Supplementary Fig. 8d), and perpendicular off-axis (Supplementary Fig. 8e). Interestingly, when the structures are allowed to energetically relax, both the parallel in-axis molecular configuration (Supplementary Fig. 8c) and the tilted configuration (Supplementary Fig. 8d) relax to parallel off-axis orientation (Supplementary Fig. 8b), indicating that these two configurations are not energetically stable. When the perpendicular off-axis configuration (Supplementary Fig. 8e) is allowed to relax, the molecular junction breaks and the molecule is adsorbed on the facet of one of the electrodes, pointing that also this configuration is instable. These observations reveal that out of the different binding possibilities
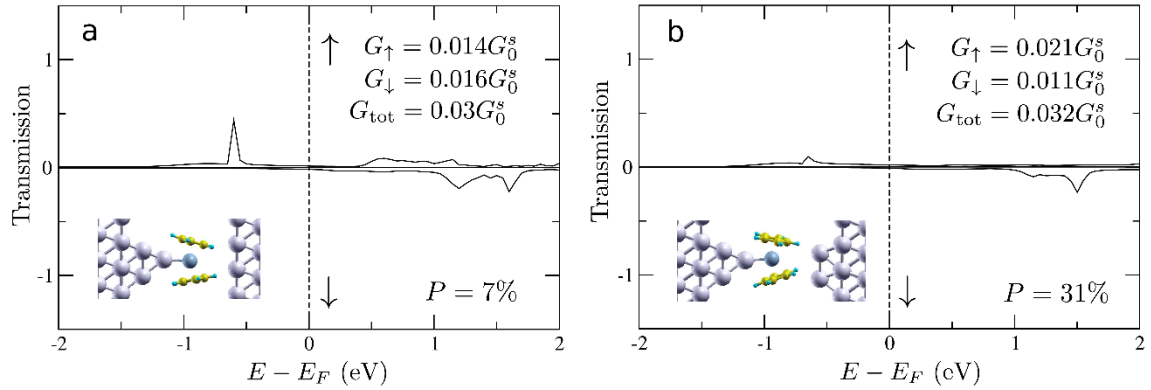
between the molecule and the electrodes considered here, only the parallel off-axis and perpendicular in-axis configurations (Supplementary Fig. 8a,b) are energetically stable. We further note that the calculated conductance and conductance spin polarization (CSP) for the configurations presented in Supplementary Fig. 8c-e deviate considerably from the experimental observations of interest, where the conductance is around $1G_0^s$ and the CSP is high. In contrast, only the perpendicular (in-axis) configuration reveals conductance and CSP that match well the mentioned experimental observations. In view of the stability of the different configurations and their transport properties, we conclude that the perpendicular in-axis and parallel off-axis configurations (denoted in the main text as perpendicular and parallel configurations for convenience) can be assigned to the experimentally found most probable high and low conductance cases, respectively. Furthermore, based on transport properties, only the perpendicular in-axis configuration can be associated with the measured high spin filtering.

Focusing on the perpendicular in-axis molecular orientation that is associated with high spin filtering, we now examine the influence of the electrode structure on the conductance (i.e., the transmission at the Fermi energy in G_0^S units) and conductance spin polarization. As seen in Supplementary Fig. 9, we find that it is enough to have one flat electrode or even one diatomic tip to lose the spin filtering effect and have a significantly lower conductance than in the experimentally observed cases of interest. This is simply due to the lack of direct binding between the vanadium atom and a protruding silver atom on each of the two electrodes that is required in order to have significant electronic transport via this pathway.

Based on the above comparison between the calculations described here and the experimental results, we conclude that the ensemble of molecular junctions that show high conductance and high spin filtering in the experiments should have the following typical structural properties: (i) perpendicular in-axis molecular orientation; and (ii) direct binding between the vanadium atom and a protruding atom on each silver electrode. The abundance of high spin filtering (for example, CSP<70%) found in the experiments together with high conductance suggests that these structural properties of the Ag/vanadocene junction are not very rare. As discussed in the main text, the significant spin filtering found for the calculated perpendicular molecular junction configuration is an outcome of spin dependent quantum interference. We note that the examination of additional archetypical structures of molecular junctions does not reveal an alternative explanation for the high spin filtering found in some of the measured molecular junctions.

Supplementary Figure 8: Calculated transmission for different molecular configurations (see Insets) in a Ag/vanadocene junction.

Supplementary Figure 9: Calculated transmission for different electrode structures (see Insets) for a perpendicular Ag/vanadocene junction.
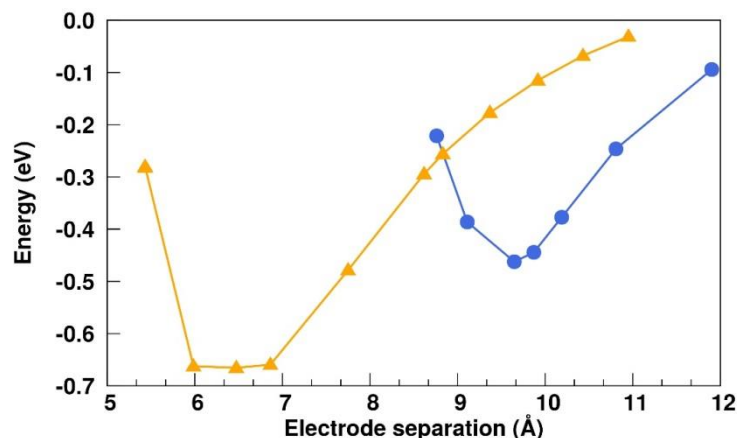
Supplementary Note 8.

Total energy and spin dependent electronic transport of Ag/vanadocene molecular junctions
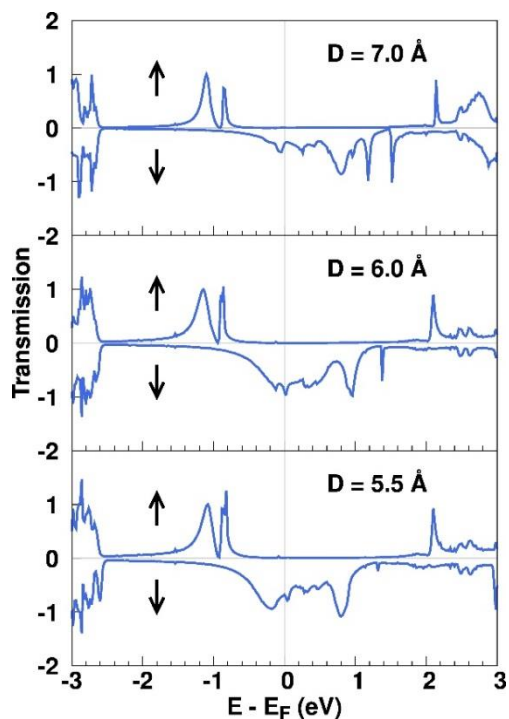
To verify that the outcome of our calculations is robust and independent of the calculation technique and methodology, we present here additional calculations done using a different methodology with respect to the calculations presented in the main text and in the rest of the Supplementary Information. Specifically, we used the SIESTA[9] and VASP[10] codes for DFT calculations, while the spin-dependent electron transport calculations were performed using a TRANSIESTA code, which is based on non-equilibrium Green's-function (NEGF) formalism with a self-consistent DFT (see Methods).

The relative stability of the parallel and perpendicular Ag/vanadocene junction configurations are presented in Supplementary Fig. 10. While the perpendicular configuration is more stable in general, the parallel configuration is more stable at a larger inter-electrode separation. Note that the most stable perpendicular orientations take place at D=6-6.8 Å, in some deviation from the calculations used in the main text and in Supplementary Fig. 12, in which the minimum energy is obtained at D= 5.8 Å, likely due to different calculation details.

The calculated spin-polarized transmission of a perpendicular Ag/vanadocene junction at different electrode separations is presented in Supplementary Fig. 11. The suppression of spin-up transmission is clearly seen for a wide energy range around the Fermi energy in all cases. In contrast, the spin-down transmission at the Fermi energy is non-monotonic with respect to electrode separation, being maximal (very close to 1) for an intermediate inter-electrode separation of 6.0 Å. This gives rise to essentially perfect conductance spin-polarization, and ideal ballistic spin-polarized transport for this junction geometry.

Supplementary Figure 10: Total energy of Ag/vanadocene junctions as a function of electrode separation. The calculations are done for perpendicular (orange triangles) and parallel (blue circles) configurations at different electrode separations. The energy axis was set to zero at the total energy of a particular configuration having two electrodes far away from each other and the molecule at the mid-point, ensuring negligible interaction between the molecule and the electrodes.
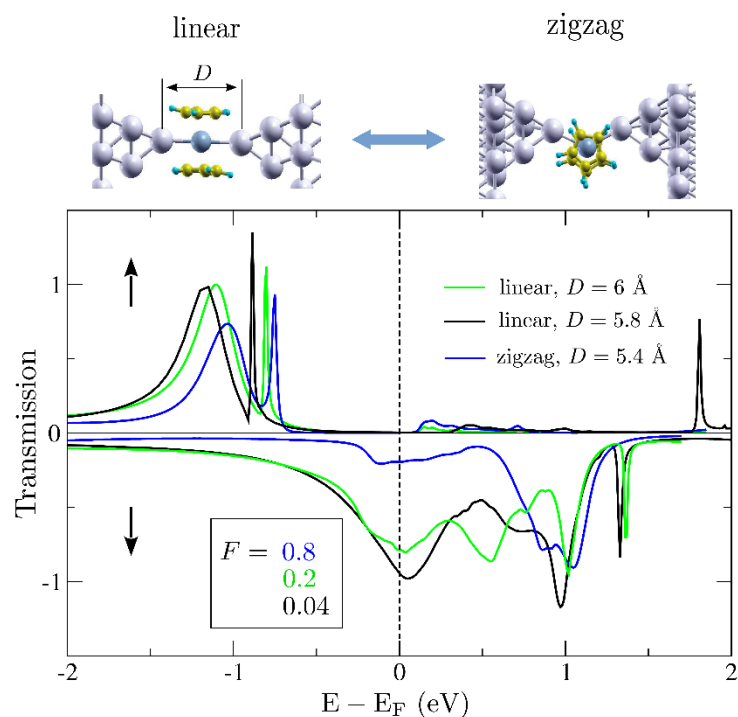

Supplementary Figure 11: Spin-resolved transmission of an Ag/vanadocene junction for perpendicular molecule orientation. Calculated transmission for spin-up and spin-down as a function of energy for perpendicular Ag/vanadocene junction configurations with different inter-electrode separations.

14

Supplementary Note 9.

Spin-resolved transmissions of perpendicular Ag/vanadocene junctions for different electrode separations

We plot in Supplementary Fig. 12 the spin-polarized transmission for different inter-electrode distance at small separation (D < 6.5 Å). The calculations are done by a homemade tight-binding code[11] with tight-binding parameters extracted from the first principles QE calculations. NEGF formalism was used to compute the spin-polarized transmission (see Methods). Two representative molecular configurations were found, namely a zigzag compact configuration at D < 5.75 Å and a linear configuration at a larger electrode separation (5.75 Å < D <6.4 Å). Note that the two carbon rings are parallel to the transport direction in both configurations. Interestingly, the spin-up transmission is always largely suppressed around the Fermi energy. The spin-down transmission at the Fermi energy, first slightly increases when reducing the inter-electrode separation - from 0.8 at D = 6 Å to almost 1 (i.e., close to ideal ballistic spin transport) at D=5.8 Å, which is the most energetically stable configuration of the junction, discussed in the main text. Then it rapidly decreases to 0.2, when the zigzag configuration is formed, reflecting much weaker hybridization between the vanadocene d_{z^2} and the s frontier states of the silver electrodes in the last case (D = 5.4 Å).

The calculations presented in Supplementary Fig. 10 and 11, as well as in Supplementary Fig. 12 and the main text were performed using different methods as described in Methods. Still, the main outcome is similar. In particular, the nearly perfect spin-filtering for the most stable perpendicular junction configuration, the significant suppression of spin-up transmission in a very wide energy window around the Fermi energy, and the non-monotonic contribution of spin-down transmission as a function of inter-electrode separation are all clearly reproduced, regardless the calculation method.
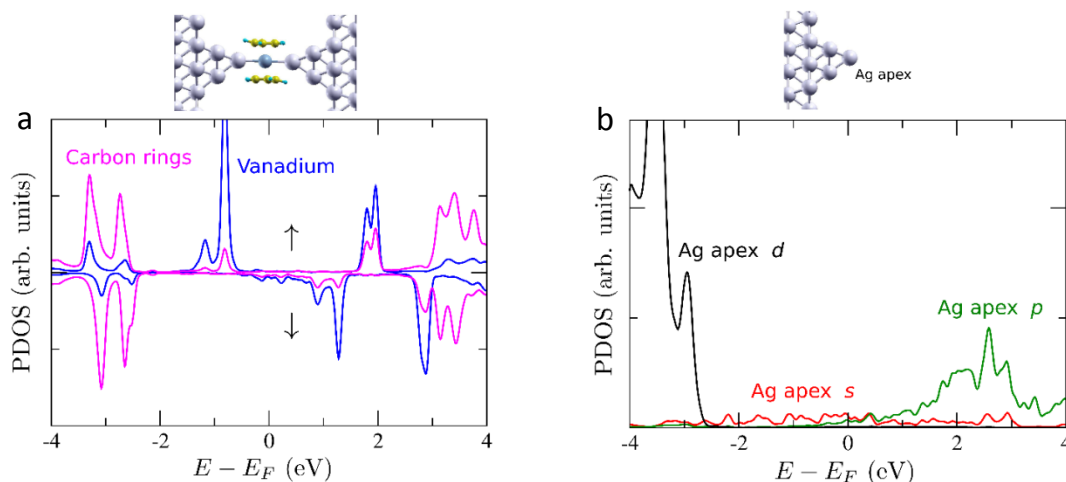
Supplementary Figure 12. Spin-resolved transmission of an Ag/vanadocene junction for perpendicular molecule orientation. Top panel: calculated junction structures for D = 6 Å and 5.4 Å (left and right, respectively). Bottom panel: calculated transmission for spin-up and spin-down as a function of energy for three different inter-electrode distances. When the linear junction is squeezed, a zigzag geometry is formed.

Supplementary Note 10.

Interference in terms of vanadium- and carbon-originated molecular states

The relevant interference takes place between the main transport contribution via the vanadium d_{z^2} level and the transport contributions from many states of the carbon rings located in a wide range of different energies. The latter states are located far from the Fermi energy at different energies, and can be clearly recognized in Supplementary Fig. 13a, at E > 3eV and E < -2eV. Our analysis (carried by switching off, one by one, different carbon states) has shown that one cannot single out a specific carbon state that dominates the interference. All these states are of importance, contributing to the efficient suppression of transmission at the Fermi energy for spin up, and to the finite phase shift in the even-symmetry scattering channel, as simulated in Supplementary Fig. 16b,c using a simple toy model.

16

Supplementary Figure 13: Calculated projected density of states. a, Calculated PDOS for Ag/vanadocene junction. The projection is on the π-system of the vanadium's carbon rings (pink) and the dz^2 orbital centered on the vanadium (blue). **b,** Calculated PDOS on different atomic orbitals located on the apex atom of a Ag electrode.

Supplementary Note 11.

The origin of the different widths for spin up and spin down transmission peaks
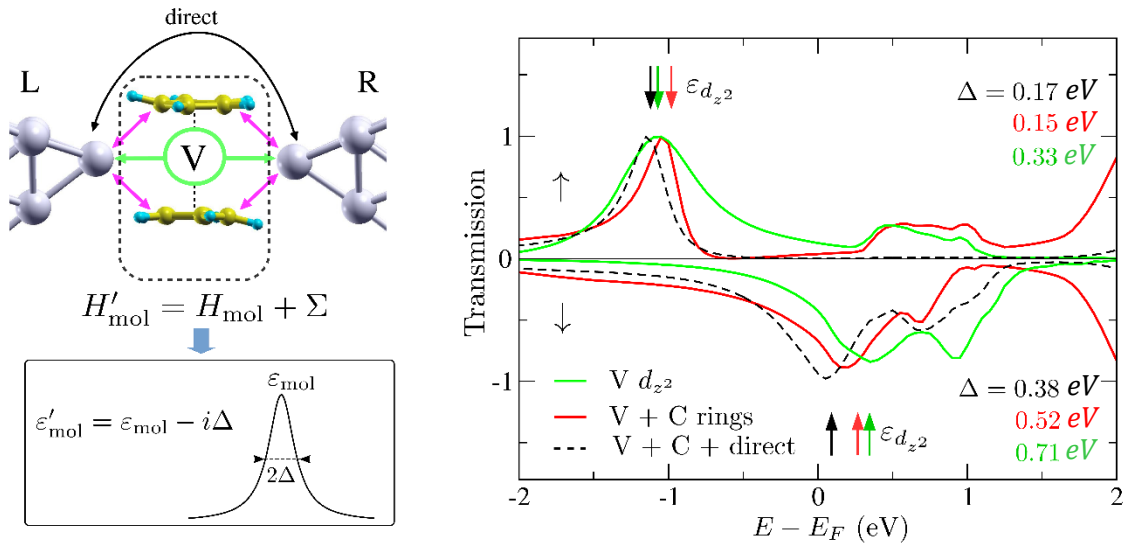
The different widths of the spin up and down transmission peaks (main text, Fig. 4) can be mainly associated with the different density of states on the apex atom of each silver electrode above and below the Fermi energy, as presented here in Supplementary Fig. 13b. Low s- density of states around E=-1.2 *eV* on the Ag tip apex results in a rather narrow transmission peak for spin up at this energy (main text, Fig. 4c; green curve). In contrast, additional Ag *p*-states appearing at E>0 close to the Fermi energy give rise to a broader transmission feature for spin down electrons at these energies (main text, Fig. 4c; green curve).

Supplementary Note 12.

The origin of the shift in the transmission peaks observed in figure 4e in the main text

In the calculations, when the vanadocene molecule is coupled to the electrodes its levels are renormalized due to the coupling matrix Σ added to the molecule's Hamiltonian H_{mol} as schematically depicted in Supplementary Fig. 14 below. The new eigenvalues of the (non-Hermitian) H'_{mol} are complex. The real term describes renormalized level positions, while the imaginary term (Δ) describes their coupling to the electrodes and defines the level's life time. The coupling matrix *Σ* is defined as *VGV*, where *V* is the hopping matrix between the molecule and the electrodes and *G* is the Green function of (the isolated from the molecule) electrodes. On the right panel of Supplementary Fig. 14 we show again the transmissions presented in the main text in Fig. 4e,

where the positions of the (renormalized) vanadium d_{z^2} - originated level (relevant for transport) are indicated by colored arrows for different coupling strengths. We see that the energy level's position (arrows) is shifted, following very well the position of the corresponding transmission peak. Thus, the shift in the transmission peak reflects change in the coupling strength of the vanadium d_{z^2} orbital to the electrodes for the tree different cases: i) coupling by only vanadium d_{z^2} - orbital to the electrodes (green); ii) coupling to the electrodes by the d_{z^2} - orbital and by the π orbitals of the carbon rings (red); and iii) direct electrode-electrode coupling is added (dashed black). The shift is due to the different coupling matrices Σ: for cases (i) and (ii), simply because of different hopping matrices V, while the electrode's Green function G is given by two independent contributions from left and right electrodes, $G=G_L+G_R$. In case (iii), the last statement is not true due to direct coupling between electrodes, so that $G=G_L+G_R+G_{LR}$ with a nonzero crossing term G_{LR}. To conclude, the shift is related to changes in the hybridization, since in each case (i-iii) different orbital combinations are taken into account, while the asymmetric shape of the transmission peaks is an outcome of the interference discussed in the main text.

Supplementary Figure 14: The role of hybridization and electrode-molecular levels coupling on the position of the transmission peaks.

Supplementary Note 13.

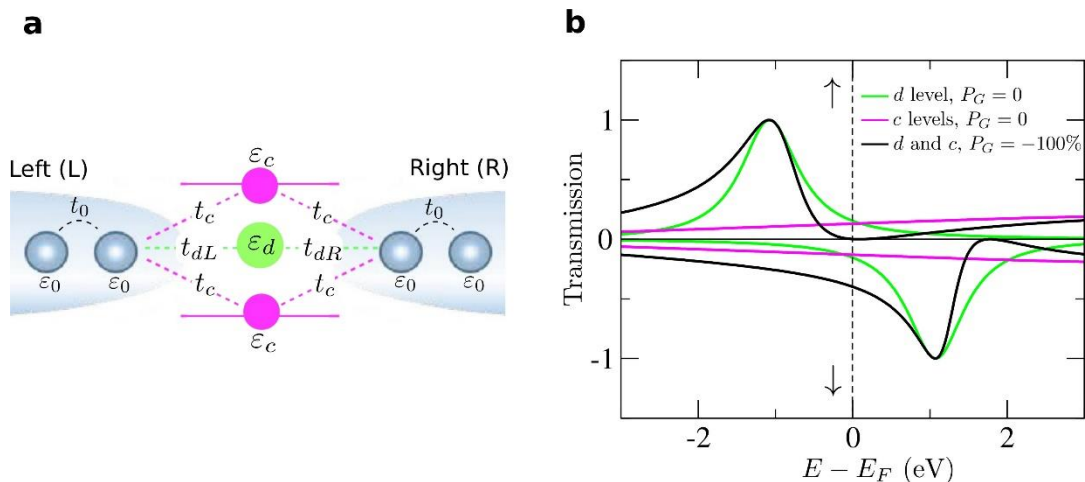**Toy model for understanding spin-dependent interference**

To illustrate the mechanism of spin filtering by quantum interference, we set up a simple tight-binding model shown in Supplementary Fig. 15. It consists of three levels: two levels simulate the energy levels of the carbon rings (at 6 eV) and one spin-split level simulates the spin-polarized d-level (d_{z^2}) of vanadium, placed symmetrically (with respect to the Fermi level) at -1 *eV* and 1 *eV* for spin-up and down, respectively. The levels are coupled to two semi-infinite 1D chains, representing the silver electrodes.

When the two pathways are treated separately, no spin filtering at the Fermi level is observed. Specifically, the transmission through the spin degenerate carbon levels (pink lines) is obviously non-polarized, while the transmission through the spin-polarized d-level (green lines) gives two spin-split Lorentzian structures with equal transmission at the Fermi energy. In contrast, if interference between the two electronic pathways is taken into account (black lines), a full reflection of spin-up electrons and enhanced spin-down transmission are found at the Fermi energy. Note that in this symmetric case (regarding the d-level spin up/down position) the perfect spin filtering at the Fermi energy is purely due to quantum interference since the d-level density of states are not spin-polarized.
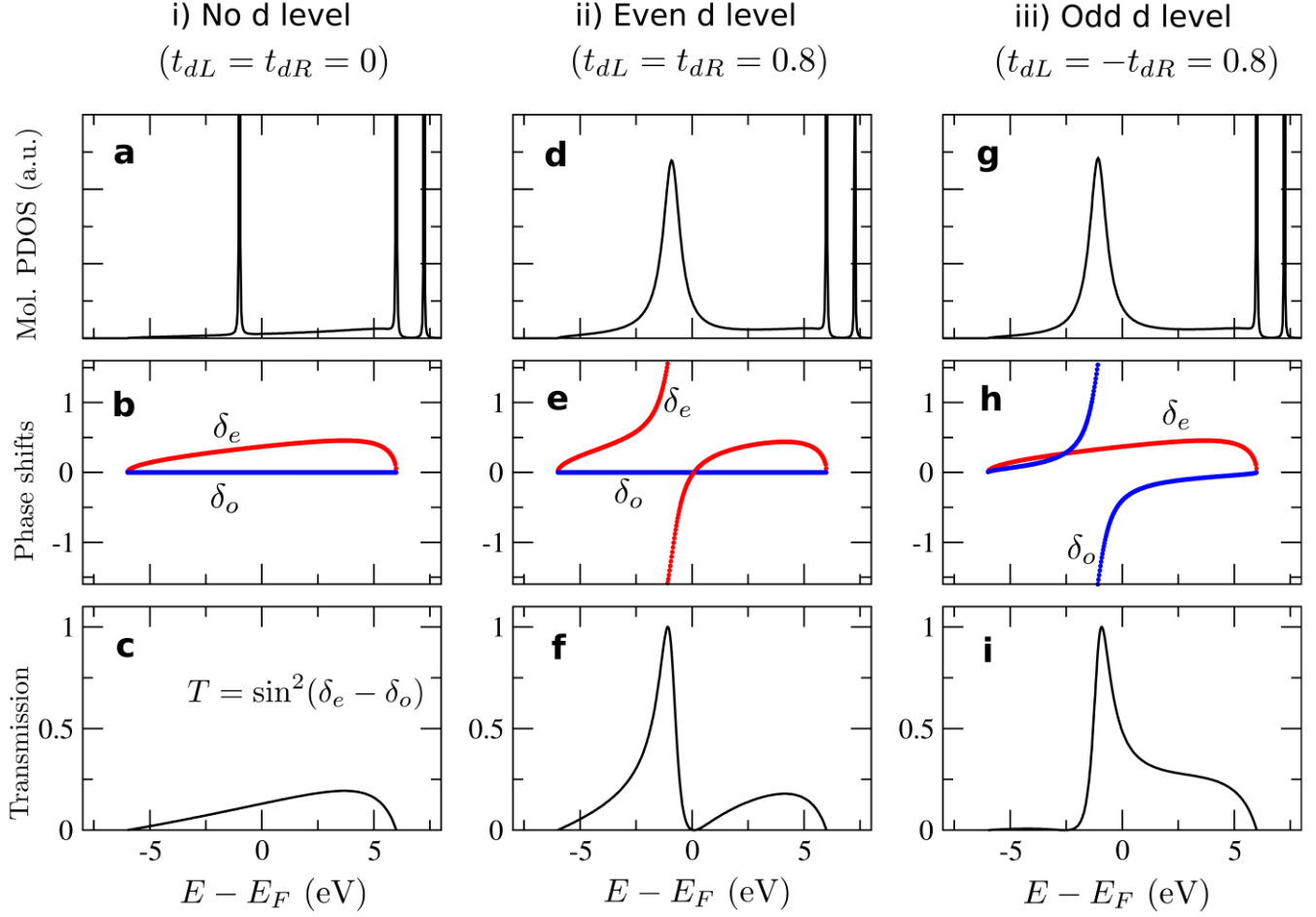
The actual asymmetric shape of the transmission function due to the above-discussed interference could be readily rationalized in terms of the so-called scattering phase shifts. In Supplementary Fig. 16, we analyze the spin-up case (as spin-down transmission has the same shape). For our single band case, the transmission probability can be expressed[12] as $T=sin^2(\delta_e-\delta_o)$, where $\delta_{e/o}$ are phase shifts in even/odd combinations of two electron waves coming from the left and from the right chains caused by a coupling to the molecule (levels). The reference system (zero phase shifts) is the one in which the two chains are fully disconnected (no molecule). Furthermore, based on Friedel sum rules, $d\delta_{e/o}(E)/dE=\pi \Delta\rho_{e/o}(E)$, where $\Delta\rho_{e/o}(E)$ are additional PDOS of even or odd symmetry (with respect to the transport direction), due to the coupling to the molecule.

When only carbon rings are coupled (symmetrically) to the chains, as presented in panels (a-c), a small (even) PDOS on the molecule is generated around the Fermi energy (a) accompanied with slowly increasing in energy δ_e (b). This situation results in a small tunneling transmission around zero energy (c). If the d-level is added with symmetric coupling to the left and right chains (as in the present case of a d_z^2 orbital), see panels (d-f), δ_e starts to increase rapidly (e) at the d-level energy, -1 eV, correlating with additional d-level derived PDOS (d); δ_o remains essentially zero. This leads to an increase of transmission to the left of the PDOS peak, while the transmission drops exactly to zero to the right when $\delta_e=\delta_o$ (f). It is interesting to note that if the d-level is coupled anti-symmetrically (for example, as in the case of a p_z orbital), (g-i), it would lead to a rapid increase in δ_o (h). Consequentially, the transmission curve would change its shape (I), and drop to zero at the left side of the PDOS peak, remaining finite at its right side.

We can conclude that the nature of interference at zero energy (at the Fermi energy) depends not only on the d-level position (with respect to the Fermi energy) but also on its symmetry. Note also that the PDOS on the molecule, on the contrary, is very similar in both cases, (d), (g).

Supplementary Figure 15. Minimal three-level tight-binding model. a, Schematic presentation of the model: *d*-level is set at -1 and at 1 eV for spin-up and down, respectively, c-levels (simulating two carbon rings) are set at 6 eV, hopping integrals are t_{dL} = t_{dR} = 0.8 eV and t_c=1.3 eV while semi-infinite electrodes are described by tight-binding chains, ε_0 = 0 and t_0 = 3 eV. **b**, Spin-dependent transmissions for two conduction pathways: one across the vanadium *d*-level (green) and one across the carbon rings (pink), as well as full transmissions (black), where both pathways are taken into consideration.

Supplementary Figure 16. Tight binding model for quantum interference patterns in the transmission. Projected density of states on the molecule (sum over all three levels), even/odd phase shifts, and the corresponding transmission functions are shown in the upper, middle, and lower panels, respectively. (i) Only the two c-levels (simulating two carbon rings) are coupled to the semi-infinite chains with t_c = 1.3 eV, (a-c); (ii) A d-level of even symmetry is also introduced, where $t_{dL} = t_{dR}$ = 0.8 eV, (d-f); (iii) The "d level" has an odd symmetry, where t_{dL} = 0.8 eV, t_{dR} = -0.8 eV, (g-i). The Fermi energy is set to zero.

Supplementary References

1. Blanter, Y. M. & Büttiker, M. Shot noise in mesoscopic conductors. *Phys. Rep.* **336**, 1-66 (2000).

2. Kumar, M., Tal, O., Smit, R. H. M., Smogunov, A., Tosatti, E. & van Ruitenbeek, J. M. Shot noise and magnetism of Pt atomic chains: Accumulation of points at the boundary. *Phys. Rev. B* **88**, 245431 (2013).

3. Roche, P., Ségala, J., Glattli, D., C., Nicholls, J., T., Pepper, M., Graham, A., C., Thomas, K., J., Simmons, M. Y. & Ritchie, D. A. Fano factor reduction on the 0.7 conductance structure of a ballistic one-dimensional wire. *Phys. Rev. Lett*. **93**, 116602 (2004).

4. DiCarlo, L.; Zhang, Y., McClure, D. T., Reilly, D. J., Marcus, C. M., Pfeiffer, L. N. & West, K. W. Shot-noise signatures of 0.7 structure and spin in a quantum point contact. *Phys. Rev. Lett.* **97**, 036810 (2006).

5. Burtzlaff, A., Weismann, A., Brandbyge, M. & Berndt, R. Shot noise as a probe of spin-polarized transport through single atoms. *Phys. Rev. Lett.* **114**, 016602 (2015).

6. Vardimon, R., Klionsky, M. & Tal, O. Indication of complete spin-filtering in atomic-scale nickel oxide. *Nano Lett*. **15**, 3894-3898 (2015).

7. Vardimon, R., Matt, M., Nielaba, P., Cuevas, J. C. & Tal O. Orbital origin of the electrical conduction in ferromagnetic atomic-size contacts: Insights from shot noise measurements and theoretical simulations *Phys. Rev. B* **93**, 085439 (2016).

8. Vardimon, R., Klionsky, M. & Tal, O. Experimental determination of conduction channels in atomic-scale conductors based on shot noise measurements. *Phys. Rev. B* **88**, 161404 (2013).

9. Soler, J. M., Artacho, E., Gale, J. D., García, A., Junquera, J., Ordejón, P. & Sánchez-Portal, D. The SIESTA method for ab initio order-N materials simulation, *J. Phys.: Condens. Matter* **14**, 2745-2779 (2002).

10. Kresse, G. & Furthmüller, J. Efficient iterative schemes for ab initio total-energy calculations using a plane-wave basis set. *Phys. Rev. B*, **54**, 11169 (1996).

11. Autès, G., Barreteau, C., Spanjaard, D. & Desjonquères. M.-C. Electronic transport in iron atomic contacts: From the infinite wire to realistic geometries. *Phys. Rev. B*, **77**, 155437 (2008).

12. Baruselli, P. P., Fabrizio, M., Smogunov, A., Requist, R. & Tosatti, E. Magnetic impurities in nanotubes: from density functional theory to Kondo many-body effects. *Phys. Rev. B* **88**, 245426 (2013).